NAG5-32
IN-48-CR

Dynamic Compensation in the Central Pacific Ocean

Juan Homero Hinojosa [1] and Bruce D. Marsh

Department of Earth & Planetary Sciences, The Johns Hopkins University
Baltimore, Maryland

([1] *Now at Department of Geological Sciences, The University of Texas, El Paso*)

ABSTRACT

The intermediate-wavelength geoid ($\lambda \sim 2000$ km) and sea-floor topography fields in the central Pacific Ocean have been studied in terms of static and dynamic compensation models. Topographic features on the sea-floor with $\lambda \leq 1000$ km have been found to be compensated both regionally, by the elastic strength of the lithosphere, and locally, by displacing mantle material to reach isostatic adjustment. The larger-scale sea-floor topography and the corresponding geoid anomalies with $\lambda \sim 2000$ km cannot be explained by either local or regional compensation. The topography and the resulting geoid anomaly at this wavelength have been modeled by considering the dynamic effects arising from viscous stresses in a layer of fluid with a highly temperature-dependent viscosity for the cases of *i)* surface cooling, and *ii)* basal heating. In this model, the mechanical properties of the elastic part of the lithosphere have been taken into account by considering an activation energy of about 520 kJ/mol in the Arrhenius law for the viscosity. Numerical predictions of the topography, total geoid anomaly, and admittance have been obtained, and the results show that the thermal perturbation in the layer, which accounts for the mass deficit, must be located close to the surface to compensate the gravitational effect of the surface deformation. For the case of basal heating, the temperature dependence of viscosity results in a separation of the upper, quasi-rigid lid from the lower mobile fluid, hence inhibiting the development of a compensating thermal perturbation at shallow depths. The results clearly rule out small-scale, upper-mantle convection as the source of these anomalies. Instead, the geophysical observables can be well explained by a shallow, transient thermal perturbation.

INTRODUCTION

Satellite radar altimetry has yielded a very accurate determination of the gravity and geoid anomaly fields over the oceans [e.g., *Marsh et al.*, 1986]. Because a gravity anomaly is an indicator of anomalous mass in a region, such information may also be obtained from a geoid anomaly, which is simply the equipotential surface produced by that anomalous mass. The geoid anomaly field has been studied to yield geophysical information ranging from the thermal evolution of the oceanic lithosphere [e.g., *Parsons & Sclater*, 1977], the mechanical properties of the oceanic lithosphere [e.g., *Watts et al.*, 1980], mantle rheology at subduction zones [*Hager*, 1984; *Richards & Hager*, 1984], to the mode of convection in the upper mantle [*McKenzie*, 1977; *Parsons & Daly*, 1983; *Buck & Parmentier*, 1986; *Hinojosa*, 1986]. This paper focuses on the high degree and order ($l,m > 12,12$) geoid field and the corresponding sea-floor topography in the central Pacific Ocean. The geoid anomaly field is characterized by east-west trending bands of alternating highs and lows with an amplitude of about 2 to 3 meters and wavelengths of about 2000-3000 km in the north-south direction. It has been suggested that perhaps shallow, small-scale mantle convection may be responsible for these anomalies [e.g., *Richter & Parsons*, 1975; *Marsh & Marsh*, 1976; *McKenzie et al.*, 1980]. However, it is important to determine what portion of the intermediate-scale geoid signal is produced by surface loads on the sea-floor before attempting to associate the total signal with upper-mantle dynamic effects. The elastic part of the oceanic lithosphere is capable of supporting short-wavelength features on the sea-floor because of its mechanical strength if

(NASA-CR-185458) DYNAMIC COMPENSATION IN THE CENTRAL PACIFIC OCEAN (Johns Hopkins Univ.) 57 p CSCL 08C

N89-26330

Unclas
G3/48 0219577

the lithosphere has cooled sufficiently. On the other hand, if the lithosphere is relatively young and weak, features on the sea-floor will adjust isostatically. These two lithospheric responses can be modeled and compared with observations of the ratio of the geoid and the sea-floor topography in the wavenumber domain, i.e., the admittance [e.g., *McKenzie & Bowin*, 1976]. We have compared the observed admittance with model admittance functions representing both regional compensation (flexure) and local compensation (Airy) to determine what part of the geoid signal results from topographic features loading the surface of the lithosphere. Once the signal associated with surface lithospheric loading has been identified, the signal arising from sub-lithospheric dynamic effects can be isolated and treated separately. The approach that we have used on the "dynamic" signal has been to consider upper-mantle fluid motions as giving rise to the sea-floor deformation and the associated geoid anomaly.

BACKGROUND

Scales of the Geoid Anomalies

The surface representing the geoid anomaly field is composed of features of many length scales (Figure 1). Because the gravitational potential decreases with distance from the source (away-from-the-source continuation), the large-scale features most likely represent very deep sources, whereas the short-scale features represent near-surface sources. *Runcorn* [1963,1964] interpreted the longest-wavelength features of the geoid in terms of sublithospheric stresses produced by convection currents in the mantle. Slightly shorter-wavelength features of the geoid have been correlated with the subduction of a cold lithospheric slab [*Chase*, 1979; *Crough & Jurdy*, 1980; *McAdoo*, 1981; *Chapman & Talwani*, 1982; *Watts & Talwani*, 1975; *Grow & Bowin*, 1975]. Even shorter-wavelength features than those associated with the subducted slabs have been used to infer the mechanical and thermal structures of the oceanic lithosphere. The study of these geoid anomalies across fracture zones [*Detrick*, 1981; *Sandwell & Schubert*, 1982; *Cazenave et al.*, 1982] provided information that distinguishes between the thermal boundary layer model [*Turcotte & Oxburgh*, 1967] and the thermal plate model [*McKenzie*, 1967] for the oceanic lithosphere, with the data favoring the plate model. The shortest-wavelength features of the geoid provide information relating to the mode of compensation of individual seamounts and oceanic islands [e.g., *Watts et al.*, 1980]. This resulted in an oceanic lithosphere model with an effective elastic thickness that increases with increasing age of the lithosphere.

The Elastic Lithosphere

Geoid anomalies are the result of surface and/or subsurface density anomalies, but the amplitude and wavelength of the anomaly can be affected by the mechanical properties of the oceanic lithosphere. The mechanical behavior of the lithosphere has been extensively modeled using a thin elastic plate approximation [*Haxby et al.*, 1976; *McKenzie & Bowin*, 1976; *Parsons & Molnar*, 1976; *Sleep & Snell*, 1976; *McAdoo et al.*, 1978; *McNutt & Menard*, 1978; *McNutt & Parker*, 1978; *McNutt*, 1984]. The elastic lithosphere, whose thickness is only a fraction of the thermal lithosphere, is defined by the depth to which elastic stress can be supported. Laboratory studies of minerals at high temperature and pressure yield the minimum temperature at which significant stress relaxation occurs. Below this temperature, the mineral behaves more as an elastic solid than a viscous fluid. Because olivine is the primary mineral in the mantle, such studies yield minimum temperatures of 475°C and 675°C for wet and dry olivine, respectively [*Turcotte & Schubert*, 1982]. The depth of these isotherms is then the elastic lithosphere thickness. *Watts et al.* [1980] found that the effective elastic thickness of the lithosphere in the Pacific, determined by applying the elastic plate theory, is bounded by the 300°C and 600°C isotherms of a cooling plate model (Figure 2). Because a given isotherm migrates downward as the lithosphere loses heat through conduction, the elastic thickness increases with increasing age of the

lithosphere. However, plate theory requires a constant value of thickness at old ages.

Scales of the Sea-floor Deformation

The intermediate-wavelength (2000-3000 km) geoid anomalies in the central Pacific offer an opportunity to infer the mode of convective instability in the upper mantle. However, they alone provide insufficient information. It is necessary to consider the deformation at the sea-floor that would be produced by the convective stresses in the upper mantle (dynamic topography), in conjunction with the geoid anomalies. These large-scale deformations are one source of sea-floor topography in the oceans. Just like the geoidal surface, the sea-floor is a surface with various scales of topography, not all of which are directly produced by upper-mantle convective stresses.

A long-wavelength source of sea-floor topography is the sea-floor subsidence, or the systematic increase in the depth of the sea-floor away from a mid-oceanic ridge crest, which has been explained in terms of simple thermal models for the evolution of the oceanic lithosphere [*Watts & Daly*, 1981]. The effects on the sea-floor topography not due to the cooling of the lithosphere can thus be isolated by removing from the bathymetry a surface obtained by using the depth-age relation. This procedure yields residual depth anomalies [*Menard*, 1973] which represent areas of anomalous topography not explained by the cooling of the oceanic lithosphere. It is these topographic anomalies which may provide useful information about convective motions in the upper mantle. However, one origin of topographic anomalies is regional changes in crustal thickness. There are topographic rises which are associated with crustal thickening, as well as topographic depressions which are associated with a thinner crust. These features can be understood in terms of Airy isostatic compensation, where a topographic load at the sea-floor is compensated at depth by a root of lower density than its surroundings.

Lithospheric Cooling and Small-scale Convection

The description of the thermal lithosphere as the upper, cold thermal boundary layer of Rayleigh-Benard convection in the mantle [*Turcotte & Oxburgh*, 1967] predicts that conductive cooling will result in lithospheric thickening and isostatic sea-floor subsidence, both effects varying linearly with the square root of age of the sea-floor [*Parker & Oldenburg*, 1973]. The associated heat flow would in turn vary inversely with the square root of sea-floor age. However, the data suggest that the sea-floor subsidence follows the predicted depth-age relation only to ages of about 80 Ma [*Sclater et al.*, 1975; *Parsons & Sclater*, 1977], and that the heat flow data fit the predictions to ages of about 50 Ma [*Sclater & Francheteau*, 1970]. Both the depth-age and the heat flow-age curves flatten to a nearly asymptotic value for older lithospheric ages. These departures from the boundary-layer-theory predictions for older lithospheric ages have been ascribed to additional heat supplied at the base of the lithosphere. A variety of mechanisms have been suggested that may supply this heat. Some of these include: viscous heating at the lithosphere-asthenosphere boundary with age [*Schubert et al.*, 1976], hot-spot lithospheric reheating [*Heestand & Crough*, 1981], and small-scale convection in the upper mantle, with horizontal dimensions much smaller than the dimensions of the plates themselves [*Richter*, 1973; *Richter & Parsons*, 1975; *McKenzie & Weiss*, 1975; *Richter & Daly*, 1978]. The high Rayleigh-number laboratory experiments of *Richter & Parsons* [1975] have shown that convective motions can occur at several horizontal scales. Further, they showed that the resulting near-surface convective motions were in the form of rolls with axes oriented parallel to the direction of motion of a moving upper boundary. *Parsons & McKenzie* [1978] argued that the time required for the formation of these convective rolls might be too long, except for the fastest-moving plates, such as the Pacific plate.

The depth of mantle convection has been a topic of much debate for some time now. The two opposing views presently held are that 1) thermal convection is shallow, and is confined to the upper 700 km of the mantle [e.g., *McKenzie et al.*, 1974]; and 2) thermal convection is deep and extends through the entire depth of the mantle [e.g., *Davies*, 1977; *Elsasser et al.*, 1979]. Much work has been

done recently on determining whether or not a second scale of convection exists in the mantle [e.g., *Parsons & McKenzie*, 1978; *Yuen et al.*, 1981; *Jaupart & Parsons*, 1985; *Yuen & Fleitout*, 1984; *Buck & Parmentier*, 1986; *Hinojosa*, 1986]. The primary concern of most of these studies was to understand the conditions under which the cold thermal boundary layer will become unstable. The results of each study depend on the rheology of the convecting layer. *Parsons & McKenzie* [1978] treated a constant viscosity layer and found that the onset of the boundary layer instability coincides with the time at which the departure from the depth-age curve is observed. *Yuen et al.* [1981] found that if the influence of temperature on viscosity is considered, fast growth rates of the instabilities can be seen if the upper-mantle viscosity is of the order of 10^{20} Poise. However, this value for the viscosity is inconsistent with the post-glacial rebound value of 10^{22} Poise [*Cathles*, 1975]. Raising the mean viscosity of the upper mantle has the effect of inhibiting the instabilities. *Jaupart & Parsons* [1985] considered a depth-dependent viscosity, and found their results consistent with the departure of the depth-age data for the sea-floor. But their model did not allow for the variation of viscosity with temperature, as should be the case for a thermally-activated creep process in the mantle. They fixed the viscosity profile to be a function of depth only, which results in a lack of interaction between the developing temperature field and the fluid flow. *Yuen & Fleitout* [1984] considered the effects of both temperature and pressure on the viscosity, and found that the instabilities can occur for mean upper-mantle viscosities of the order of 10^{22} Poise, but that the growth rate peaks at young ages (<50 Ma), and decreases thereafter with time, just the opposite effect of what is thought to explain the depth-age curve flattening in the first place. *Buck & Parmentier* [1986] studied the development of small-scale instabilities under a young lithosphere being cooled from above by using a two-dimensional numerical model which includes a temperature- and pressure-dependent viscosity. Their goal was to explain the existence of short and fairly uniform wavelength (<200 km) gravity anomalies in the central east Pacific observed by *Haxby & Weissel* [1986]. These anomalies are said to persist to crustal ages of 50 Ma. Buck & Parmentier find that the dominant wavelength of the predicted gravity anomalies increases from about 80 km after 2 Ma to 200 km after only 10 Ma, and that the amplitude of the predicted anomalies is close to that of the observed anomalies if flexural damping by the lithosphere is neglected. However, as their calculations continue to evolve in time, the vertical and horizontal length scales of the convection cells also increase with time. They do not explicitly mention just what wavelength is reached as the calculation is carried out in time.

The presence of such small-scale convection in the upper mantle would produce lateral density heterogeneities which should be reflected in the gravity field. *Marsh & Marsh* [1976] first noticed an east-west pattern in the gravity field of the central Pacific Ocean with a north-south wavelength of about 2000 kilometers after examining the PGS-110 free-air gravity anomaly map relative to the degree and order 12 field model. They proposed that this pattern might be representative of a second scale of convective motions confined to the upper mantle. This same pattern can be seen in the geoid anomaly map of Figure 3. This figure shows the residual geoid anomalies after removing the Goddard Earth Model (GEM) 10B gravimetric geoid field model [*Lerch et al.*, 1982], up to degree and order 12, from the full SEASAT geoid. This map contains geoid anomalies with wavelengths shorter than about 3300 km. The geoid highs are in white and the geoid lows are in gray, with a contour interval of 2 meters. The amplitudes of these anomalies are about 2 to 3 meters, and they appear to be somewhat elongated in the direction of plate motion, analogous to what was observed experimentally by *Richter & Parsons* [1975]. A simple stability analysis led *Parsons & McKenzie* [1978] to conclude that thermal instabilities could develop on the cold thermal boundary layer at ages greater than about 80 Ma, where cold material descends and is immediately replaced by hot material from below, with this cycle continuing as the lithosphere continues to cool. But because the linear geoid anomalies extend towards the younger sea-floor, instabilities which develop at later ages will not explain the younger portion of the geoid anomalies. To correct for this inconsistency, *McKenzie et al.* [1980] proposed that instabilities on a lower hot thermal boundary layer at a depth of about 700 km would rise and appear below the young sea-floor, thus producing the continuous pattern from young to old sea-floor.

Models of Isostatic Compensation

To decide on the origin of a topographic anomaly, the mode of isostatic compensation must be inferred by observing the correlation between sea-floor topography and geoid anomaly. The approach often used to accomplish this is the transfer function technique, where the data are treated as time series, or spatial series. *Dorman & Lewis* [1970,1972] first used time series techniques to analyze the relationship between gravity and topography of the continental United States. Later, *McKenzie & Bowin* [1976] applied time series analysis to gravity and bathymetry profiles in the Atlantic Ocean. Treating the bathymetry as a discrete input signal and the gravity anomaly profile as a discrete output signal, they obtained information about the thickness of the oceanic lithosphere at mid-oceanic ridges. Others used transfer function techniques to further investigate the lithospheric properties at mid-oceanic ridges [e.g., *Cochran, 1979; McNutt, 1979; Cazenave et al., 1983*]; whereas the properties of the oceanic lithosphere at aseismic ridges have been studied by *Watts* [1978] and *Detrick & Watts* [1979]. The ratio of the Fourier transformed geoid anomaly data to the Fourier transformed sea-floor topography data is the observed admittance. The admittance represents the amplitude of the resulting geoid anomaly per unit amplitude of the sea-floor topography, at a given wavelength. However, the observed admittance is two-dimensional and complex, but the isostatic response of the earth is assumed to be isotropic and real. Therefore, the admittance obtained from the data must be averaged in radial rings of width Δk in the wavenumber domain. The observed admittance can be computed by using

$$Z(|k|) = \frac{<Re(N(k)H^{*}(k))>}{<|H(k)|^{2}>} \qquad (1)$$

where $N(k)$ is the geoid anomaly spectrum, $H(k)$ is the sea-floor topography spectrum, * denotes complex conjugation, and the angle brackets denote radial averaging. (We used a value of Δk equal to twice the fundamental wavenumber in the averaging). The observed admittance can then be compared with model admittance functions, in the wavenumber domain, which are derived from simple models of isostatic compensation, the two most often used being Airy (local) isostasy and flexure (regional) isostasy. In Airy isostasy, the mantle underneath a surface load is displaced to accommodate the load. The Airy admittance function is given by

$$Z_{A}(|k|) = \frac{2\pi\Gamma}{g_{o}|k|}(\rho_{c}-\rho_{w})e^{-|k|s}(1-e^{-|k|d}) \qquad (2)$$

where Γ is the universal gravitational constant, ρ_{w} is sea-water density, ρ_{c} is oceanic crustal density, ρ_{m} is mantle density, s is the mean sea-floor depth, d is the mean oceanic crust thickness, g_{o} is the mean value of the acceleration of gravity, and $|k|$ is the magnitude of the wavenumber.

In regional isostasy, the elastic part of the lithosphere, which grows with age of the sea-floor [*Watts et al., 1980*], can help support a load by providing an elastic restoring force, in addition to the buoyancy force of the low density root. The flexure admittance function is given by

$$Z_F(|k|) = \frac{2\pi\Gamma(\rho_c-\rho_w)e^{-|k|d}}{g_o|k|}\left[1-\left[1+\frac{D|k|^4}{(\rho_m-\rho_c)g_o}\right]^{-1}e^{-|k|d}\right] \quad (3)$$

where all of the parameters are as defined before, and D is the flexural rigidity of the elastic lithosphere defined by

$$D = \frac{ET_e^3}{12(1-\nu^2)} \quad (4)$$

where E is Young's modulus, ν is Poisson's ratio, and T_e is the effective elastic thickness. Depending on the age of the lithosphere, the elastic part of the lithosphere can support topographic loads smaller than a given wavelength called the flexural wavelength. Loads with wavelengths greater than the flexural wavelength will not be fully supported, and will result in Airy-type isostatic adjustment. Using a typical value of 20 km for the lithospheric elastic thickness [*Watts*, 1978], the corresponding value for the flexural wavelength is about 386 km. Full isostatic adjustment can be shown to occur for wavelengths greater than about 660 km for this value of elastic thickness. But if the lithosphere has essentially no strength for static surface loads of wavelengths greater than about 660 km, the same must hold true for dynamic stresses of convective origin applied at the base of the lithosphere. The consequence of this lack of strength is that we can expect the long-wavelength sea-floor topography to be either Airy compensated or produced by upper-mantle convective motions of the same wavelength. Conversely, any sub-lithospheric stress distribution of short wavelength (shorter than the flexural wavelength) will not be transmitted to the surface. Thus, the elastic lithosphere acts as a low-pass filter of the stress distribution at the base of the lithosphere.

The response of the elastic lithosphere to an applied surface load is contained in the admittance function. In the limit of zero-elastic strength, the admittance is the Airy admittance function. For a finite elastic strength, the response of the lithosphere is regional. Figure 4 shows the isostatic response of a zero-strength elastic plate, which results in complete isostatic compensation for all-wavelength loads. The values of the physical parameters used to obtain these curves are listed in Table 1. These curves give the resulting geoid anomaly (in meters) for every kilometer of sea-floor topography, at a given wavelength. The number next to each curve is the depth of compensation in kilometers.

TABLE 1. Airy Model Parameters

Parameter	Symbol	Value
Sea-water density	ρ_w	$1.025\ g\ cm^{-3}$
Oceanic crustal density	ρ_c	$2.800\ g\ cm^{-3}$
Mean sea-floor depth	s	$4668\ m$
Universal gravitational constant	Γ	$6.67 \times 10^{-8}\ cm^3\ s^{-2}\ g^{-1}$
Acceleration of gravity	g_o	$980\ cm\ s^{-2}$

The isostatic response of a finite-strength elastic plate is shown in Figure 5, with the physical parameters listed in Table 2. The number next to each of these curves is the effective elastic plate thickness in kilometers. Note the response for the extreme cases of very-long and very-short wavelength topography. The long-wavelength case reflects the local isostatic adjustment due to the bending of the elastic plate. In the short-wavelength case, the elastic plate can fully support the surface load, but the attenuation of its gravitational signal across the oceanic water column gives a low value for the admittance. In the intermediate range, the plate begins to bend while still supporting part of the load (regional compensation), but the gravitational signal of the load is attenuated less, hence a larger value for the admittance. Using these expressions, one can extract the depth of compensation in the case of Airy isostasy, and an effective elastic thickness for the lithosphere which relates to its flexural rigidity in the case of regional compensation.

TABLE 2. Flexure Model Parameters

Parameter	Symbol	Value
Sea-water density	ρ_w	$1.025\ g\ cm^{-3}$
Oceanic crustal density	ρ_c	$2.800\ g\ cm^{-3}$
Sub-crustal mantle density	ρ_m	$3.300\ g\ cm^{-3}$
Mean sea-floor depth	s	$4668\ m$
Universal gravitational constant	Γ	$6.67 \times 10^{-8}\ cm^3\ s^{-2}\ g^{-1}$
Acceleration of gravity	g_o	$980\ cm\ s^{-2}$
Poisson's ratio	ν	0.25
Young's modulus	E	$10^{12} g\ cm^{-1}\ s^{-2}$

DESCRIPTION OF DATA AND STUDY AREA

SEASAT Geoid Anomalies

The radar altimeter of the SEASAT satellite was used to record the instantaneous altitude of the satellite over the oceans, from which the geoid can be directly derived by determining the orbital position of the satellite from tracking stations (cf. Fig. 1) [*Marsh et al.*, 1986]. The measurements taken by the SEASAT altimeter covered a period of 18 days from July 28 to August 15, 1978. The altimeter took 1000 radar measurements per second, which were smoothed to produce values at one second intervals (corresponding to about 7 km along a satellite ground track), with a resulting precision of about 10 cm [*Marsh & Martin*, 1982]. Because this study deals with the intermediate-wavelength features of the geoid, it is necessary to remove the long wavelengths. To achieve this, the Goddard Earth Model (GEM) 10B gravimetric geoid field model [*Lerch et al.*, 1982], up to degree and order 12, has been removed from the full geoid (cf. Fig. 3). The sampling interval of the SEASAT data used is 1° in latitude and longitude.

SYNBAPS Bathymetry

The data set used to derive the sea-floor topography is the Synthetic Bathymetric Profiling System (SYNBAPS) values obtained from the U.S. Naval Oceanographic Office (U.S.N.O.O.). The SYNBAPS bathymetry values are not actual recorded depths, but instead are values digitized and gridded from bathymetric contour charts. Data are created by interpolation where observations are sparse, and regional trends are extrapolated so as to construct a continuous representation of the bathymetry. The charts used were large to medium scale (1:1,000,000 or larger) publications of the U.S.N.O.O. This procedure undoubtedly makes the high frequency data unreliable. However, since this study concentrates on the longer wavelength data, errors in the high frequencies will not affect the

results. The sampling interval of the SYNBAPS data used is 1° in latitude and longitude.

Study Area

The study area is a 3,100 *km* × 3,100 *km* region in the central Pacific Ocean extending in longitude from 205° to 236°, and in latitude from - 13° to 18°. Figure 6 shows a map that locates the study area, and the bathymetry appears in Figure 7. The bathymetric features in the region include the Marquesas hot-spot swell at (220°,- 9°); two minor basins at (213°,- 8°) and (228°,- 8°); minor rises at (209°,0°) and (220°,3°); a plateau at (222°,14°); a depression at (207°,14°); plus a number of major fracture zones being nearly equidistant with a separation of about 1000 km, and running in a nearly east-west direction. The age off-sets of the major fracture zones can be seen in Figure 8, which shows the age of the sea-floor in Ma. This map was obtained by digitizing the age map of *Pitman et al.* [1974]. It can be seen that the average age off-set across these fracture zones is about 10 Ma, and that the age of the sea-floor increases westwardly from about 30 to 90 Ma in the study area.

The depression at (207°,14°) seems to be associated with the flexure of the lithosphere due to the Hawaiian swell, whereas the rise at (209°,0°) seems to be an extension of the Line Islands. To a certain degree, these features are all reflected in the high degree and order geoid (cf. Fig. 3).

RESULTS

Spectral Analysis

Ordinarily, both geoid anomalies and bathymetry are corrected for the subsidence of the oceanic lithosphere due to cooling (thermal isostasy). Because a cooling half-space model predicts the observed subsidence in sea-floor depth, this correction is made by applying a relation in which the depth of the sea-floor increases with the square root of the age of the sea-floor [*Parsons & Sclater*, 1977]. On the other hand, the geoid anomaly varies linearly with the age of the sea-floor at a rate of about 0.16 m/Ma if the cooling half-space is used [*Haxby & Turcotte*, 1978]. These operations are equivalent to removing the trend from the data. But, because the lower harmonics ($l,m < 13,13$) have been removed from the geoid anomaly field, it is not clear that removal of the depth-age relation from the bathymetry will result in a field that can be directly compared with the geoid. To avoid this ambiguity, each data set was prepared as follows:

(i) The shortest wavelengths were removed by smoothing in the space domain. This operation is necessary to satisfy the sampling theorem [e.g., *Bloomfield*, 1976];

(ii) A mean depth of -4668 meters was removed from the bathymetry;

(iii) The bathymetry was passed through a Gaussian filter of the form

$$F(|k|) = \exp\left[\frac{-|k|^2\beta^2}{4}\right] \qquad (5)$$

where $|k|$ is the magnitude of the wavenumber, and β is the half-width of the Gaussian filter. A value of β = 1000 km was used to low-pass filter the bathymetry, which was then removed from the full bathymetry, thus yielding the "sea-floor topography" used in this study (Figure 9). To reduce leakage, the borders of both data sets (10% of the data on each border) were cosine-tapered before taking the two-dimensional discrete Fourier transform. To obtain the isostatic response of the lithosphere, it is

assumed that the

The average estimate of the admittance between the geoid anomaly field and the sea-floor topography field was calculated as described above, and is shown in Figure 10, together with one standard deviation uncertainties. To see whether the admittance is in fact real valued, the phase of the admittance was calculated by using

$$\phi(k) = Tan^{-1}\left[\frac{Im(Z)}{Re(Z)}\right] \tag{6}$$

Figure 11 shows the phase spectrum of the admittance. For wavelengths shorter than about 1700 km, the phase is close to zero, and the admittance can be considered to be real.

Another quantity that is of importance is the coherence. The coherence is a measure of the fraction of the observed geoid at a given wavelength that can be directly related to the sea-floor topography, and is given by

$$\gamma^2(k) = \frac{< |N(k)H^*(k)| >^2}{<N(k)N^*(k)><H(k)H^*(k)>} \tag{7}$$

where all the quantities are as defined above. Figure 12 shows a plot of the coherence between the geoid and the sea-floor topography against wavelength. The coherence is high (>0.5) for the whole spectrum of wavelengths analyzed, which implies that, at a given wavelength, the geoid anomaly correlates positively with the topography.

Except for the very long wavelengths (> 1700 km), the observed admittance has a value of less than 4 m/km. For the waveband between about 350 and 400 km, flexure admittance model curves with elastic plate thicknesses of 15 and 23 km bracket the data, with a best-fitting value of 19 km. On the other hand, the data in the waveband between about 400 and 1000 km are bracketted by 20 and 30 km flexure curves, with a best fit of 25 km (Figure 13). The fact that there are two average values for the elastic thickness can be understood by recalling that the sea-floor age in the study area varies from about 30 to 90 Ma, with corresponding effective elastic plate thicknesses of 16 to 28 km, respectively [*Watts*, 1979].

The values of the admittance for wavelengths shorter than about 350 km lie on an Airy admittance curve with an average crustal thickness of about 25 km (Figure 14). This value for the crustal thickness is not unreasonable in light of *Detrick & Watt's* [1979] conclusions that some topographic features form on or near a ridge axis where the lithosphere is hot and relatively weak, thereby allowing an overthickening of the oceanic crust. As the lithosphere cools and the features move away from the ridge, the local compensation is "frozen in", and the mode of isostasy will persist, showing up as a geoid anomaly of relatively small amplitude. It is, thus, clear that topographic features on the sea-floor with wavelengths shorter than about 1000 km are in isostatic equilibrium compensated both regionally and locally.

ORIGINAL PAGE IS
OF POOR QUALITY

For wavelengths longer than about 1700 km, the observed admittance is relatively large (about 6 to 8 m/km). Clearly, neither Airy nor regional compensation can explain the long-wavelength response of the lithosphere observed in the central Pacific. By keeping in mind that the concept of isostasy requires essentially a dipolar distribution of mass, the fact that Z is large implies that the compensating mass anomalies for features at these wavelengths are deep in the lithosphere, but more likely below it.

Those features with wavelengths between about 1000 and 1700 km are also not compensated by either an Airy or a flexural mechanism, but may result from the same sub-lithospheric processes as the lower-harmonic anomalies.

Test for Reliability of the Truncated Geoid

It is common practice to remove the very long-wavelength features from the geoid to expose density heterogeneities at shallower depths. This is done by removing a field model of low degree and order from the full geoid [e.g., *Marsh & Marsh*, 1976; *McKenzie et al.*, 1980; *Watts et al.*, 1985]. However, *Sandwell & Renkin* [1988] attribute the geoid features with wavelengths of about 3500 km not to a physical source, but to leakage effects caused by using a truncation filter on the field model to a given degree and order. If this is the case, then the spectrally-derived value for the admittance of between about 6 and 8 m/km at the long-wavelength end of the admittance spectrum would be an over-estimate of the actual admittance. To test the reliability of that estimate, the admittance of the geoid and topography fields was calculated in the spatial domain starting with the full, unfiltered geoid and bathymetry fields. A surface of a given degree was fitted and removed from the full SEASAT geoid and bathymetry data. After removing the n^{th} degree surface fit from both the geoid and the bathymetry, the resulting fields were 5-point smoothed to remove the short-wavelength features. Contour maps of the resulting geoid anomaly fields for the first to the third degrees are shown in Figures 15-17. The corresponding sea-floor topography fields did not change much from surface to surface, and only the topography resulting from the removal of a cubic surface is shown in Figure 18. A scatter plot of the fields generated by using the cubic-surface fits was produced and is shown as Figure 19. Note that there is a nearly linear dependence of the geoid on the topography, as can be evidenced by the linearity in the high density nucleus of data points. As with any two-dimensional data sets there cannot be a perfect correlation because of the noise which is inherent in the data. This noise appears on the scatter plot as a halo surrounding the linear nucleus. The correlation coefficient between the two fields is about 0.66, which is significant. The admittance can be obtained from this plot by noting that it is simply the slope of the linear trend. The slope of the best-fitting line is about 7.5 m/km, a value very close to the spectrally-derived values. From this comparison we can conclude that the long-wavelength admittance function has been reliably obtained, and that it reflects a sub-lithospheric source of compensation.

A mechanism which has not been discussed thus far is the dynamic support of sea-floor topography by stresses associated with upper-mantle convective motions. These sub-lithospheric contributions to the sea-floor topography and geoid anomaly fields will be addressed more fully in the following sections.

Dynamically Supported Anomalies

We have studied the relationship between the intermediate-wavelength SEASAT geoid (λ < 3300 km) and filtered sea-floor topography fields in the central Pacific Ocean in terms of the isostatic response of the lithosphere. We have found that topographic features on the sea-floor with wavelengths shorter than about 1000 km are compensated both locally, and regionally by the strength of the elastic lithosphere (Figure 13). However, the larger-scale sea-floor topography and the corresponding geoid anomalies with a wavelength of about 2000 km cannot be explained by either local or regional compensation, as evidenced by the large mean value of the observed admittance. The deep-seated density anomalies which must exist to compensate the long-wavelength features of the

sea-floor are here considered to be the result of upper-mantle convective flow in a layer of highly temperature-dependent viscous fluid with different combinations of heating from below and cooling from above. Three cases were considered:

1) cooling from above with low activation energies;
2) heating from below with the inclusion of a low viscosity zone for
   a) mean upper-mantle viscosity of 10^{22} Poise,
   b) mean upper-mantle viscosity of 10^{21} Poise;
3) cooling from above with a low viscosity zone and with the thermal perturbation localized close to the base of the lithosphere.

The geophysical quantities desired for comparison with the observables are the geoid anomaly and the sea-floor topography, which are numerically calculated. The model must be able to simultaneously predict a geoid anomaly with an amplitude between 2 and 3 meters, a topography amplitude between 0.25 and 0.3 km, and an average admittance of between 6 and 8 m/km, as derived both spectrally and spatially. Table 3 summarizes the observational constraints which must be satisfied by the upper-mantle convection model.

TABLE 3. Observational Constraints on Convection Model

Quantity	Symbol	Value
Wavelength	λ	2000 *km*
Geoid	N_T	2 - 3 *m*
Topography	w_o	0.25 - 0.3 *km*
Admittance	Z	7.5 *m /km*
Activation energy	Q	526 *kJ /mol*
Upper-mantle viscosity	η_∞	10^{22} *Poise*

The geoid anomaly is the resultant of three contributions: i) the effect due to the top boundary deformation, ii) the effect due to the bottom boundary deformation, and iii) the effect due to the internal density anomalies arising from the thermal variations of the fluid in the convecting layer. The topography is the amount of deformation of the top boundary due to the normal stress distribution at the base of the lithosphere arising from the buoyancy of the viscous material in the layer.

Consider the model of the oceanic lithosphere and the underlying upper mantle shown in Figure 20. In this model, small-scale convective motions having the form of rolls with axes oriented parallel to the direction of plate motion are assumed to be capable of developing in a variable-viscosity, infinite Prandtl number fluid. The depth of the layer is taken to be 700 km, which is approximately the depth at which the seismic discontinuity, ~~believed to be~~ due to a compositional change, occurs. The

wavelength of the fluid motion is fixed at 2000 km, which corresponds to the dominant wavelength in the central Pacific.

The viscosity of the fluid throughout the layer is assumed to be a strong function of temperature, varying exponentially with inverse absolute temperature, the so-called Arrhenius law. The dynamic viscosity is given as a function of absolute temperature by

$$\eta(T) = \eta_o \exp\left[\frac{Q}{RT}\right] \tag{8}$$

where η_o is a reference viscosity, Q is the activation energy, and R is the universal gas constant. By using this form for the viscosity, a high-viscosity, quasi-rigid lid develops and evolves as the cold thermal boundary layer grows with time. In this lid, the velocities are vanishingly small, and the circulation is confined to the low-viscosity fluid below the lid.

The thermally-activated creep of mantle rock depends on the activation energy, Q, which is a measure of the sensitivity of viscosity to temperature. The higher the value of Q, the more sensitive the viscosity will be to any variations in temperature. To keep the viscosity in the lid from blowing up as the temperature approaches the upper-boundary temperature, a cut-off temperature defining a mechanical boundary layer is used. At temperatures below this cut-off temperature, the viscosity of the lid is held constant.

The dynamic viscosity can be written as a viscosity contrast by expressing the viscosity at temperature T relative to the viscosity at the temperature of the lower boundary (T_o) as follows

$$\frac{\eta}{\eta_o} = \exp\left[\frac{Q}{R}\left(\frac{1}{T} - \frac{1}{T_o}\right)\right] \tag{9}$$

As the temperature decreases from the lower-boundary temperature, the viscosity contrast increases from a value of unity to a maximum value specified by the viscosity of the lid at the cut-off temperature. For heating from below, a reference viscosity, η_{oo}, of 10^{22} Poise at a temperature of 1300°C will be used.

The equations expressing conservation of mass, momentum, and energy in an infinite Prandtl number fluid layer with variable viscosity have been numerically solved using the single-mode, mean-field approximation [e.g., *Olson*, 1981]. The development of the governing equations can be found in Appendix A. The expressions for the net, or total, geoid anomaly and surface deformation resulting from the convective motions have been derived in Appendix B. The solutions to Eqs. (A15)-(A16), subject to the boundary and initial conditions (Eqs. (A17)-(A18)), have been obtained numerically by using a computer code provided by Dr. Peter Olson. The values of the physical parameters used are given in Table 4.

TABLE 4. Upper-mantle Convection Parameters

Parameter	Symbol	Value
Upper-mantle density	ρ_m	$3.5\, g\ cm^{-3}$
Acceleration of gravity	g_o	$1000\ cm\ s^{-2}$
Coefficient of thermal expansion	α	$3.0 \times 10^{-5}\ C^{-1}$
Thermal diffusivity	κ	$8.0 \times 10^{-3}\ cm^2\ s^{-1}$
Reference viscosity	η_{oo}	10^{22} *Poise*

Case 1

The quantities characterizing the evolution of the flow and heat transport are shown in Figures 21-25 as profiles across the layer for case 1. These quantities were calculated using a lower-boundary temperature of 1300°C (Ra = 585,000) and a cut-off temperature of 450°C, at which point the viscosity contrast was fixed at 100 (i.e., Q = 51 kJ/mol). The adiabatic increase in temperature has been ignored in all of the calculations. The solutions were monitored at Fourier times of $\kappa t / d^2$ = 0.001 (dotted line), 0.002 (dashed), 0.003 (dot-dash), 0.004 (long dash-dot), and 0.005 (dash-dot-dot-dot).

In Figure 21, the mean temperature is shown, with both the height and temperature axes normalized to unity. The mean temperature of the fluid in the layer remains very nearly constant, except at points close to the top boundary where large temperature gradients occur, representing the loss of heat out of the top boundary. The temperature curve migrates downward with time as the fluid continues to cool. Note that the advection term in Eq. (A16a) has little effect, resulting approximately in the error function solution.

Figure 22 shows the viscosity contrast across the layer, defined as the ratio between the viscosity at a given point and the viscosity at the lower-boundary temperature (which is fixed at 10^{22} Poise to conform with post-glacial rebound data). Note that because the viscosity is only a function of the mean temperature, the shape of the viscosity curve follows that of the mean temperature curve, but in reciprocal fashion, so that the viscosity contrast increases as the mean temperature decreases. Hence, the viscosity contrast profile also shows very large gradients close to the upper boundary, with a quasi-rigid lid forming on the coldest regions of the fluid. This lid grows with time as the fluid continues to cool, and is evidenced by the downward migration of the viscosity contrast curve with time, thereby reducing the amount of low-viscosity fluid available for fluid motion to occur.

Figure 23 shows the fluctuating temperature component with the axes scaled as in Figure 21. Again, the solution is monitored at the same times as described above. The fluctuating temperature is the thermal perturbation which provides the buoyancy to drive the fluid flow. For this case, the fluctuating temperature peaks just below the thermal boundary layer, and its amplitude increases with time as it migrates downward. The downward migration of the peak occurs because the growth of the boundary layer lowers the hot, low-viscosity material where the temperature disturbance can grow.

The horizontal and vertical velocity profiles appear in Figures 24 and 25, respectively. The velocities first slowly diminish then rapidly increase with time. Note that the velocities diminish in the cold, quasi-rigid lid at the upper boundary which develops in response to cooling. If the viscosity is large in this cold region, the transfer of heat will be purely by conduction, whereas below this region heat is transported by convection.

Figure 26 shows the geoid components as a function of age of the sea-floor calculated using the parameters as in Figures 21-25. The open triangles represent the calculated values at equal intervals of time. The largest component is the upper-boundary-deformation anomaly (dotted line) because it is minimally attenuated across the water column. The smallest component is the lower-boundary-deformation anomaly (dot-dash line) because its effect is strongly attenuated across the fluid layer and water column. This component is about 1/2% of the upper component, and is hence not very significant. On the other hand, the thermal component (dashed line) can be seen to be more important. It gradually increases in magnitude due to an increase in the fluctuating temperature with time. The thermal component constitutes about 50% of the upper component at later times, but of opposite sign, hence reducing the total geoid anomaly (solid line).

The total geoid anomaly, the upper-boundary deformation, and the admittance were also calculated for activation energies between 51 and 154 kJ/mol. The reason for using low activation energies is to investigate the effect that a negligible mechanical lid has on the derived quantities. Figures 27 and 28 show the total geoid and the topography as a function of age for activation energies in kJ/mol of 51 (dotted line), 77 (dashed), 102 (dot-dash), 128 (long dash-dot), and 154 (dash-dot-dot-dot). For the lowest activation energy the viscosity of the mechanical lid is only about two orders of magnitude larger than that in the core of the fluid. Hence, the normal viscous stress can be rapidly transmitted to the surface through the thermal boundary layer. It can be seen in Figure 25 that the normal viscous stress at the surface first decreases then increases in magnitude as time increases. This accounts for the increase in both the geoid and the topography with time. As the activation energy is increased, however, the viscosity of the fluid becomes more sensitive to the temperature variations, and although the thickness of the mechanical lid is small, the viscosity gradient in the thermal boundary layer becomes very large. This increase in the gradient of the viscosity makes the velocity components decrease rapidly in the thermal boundary layer, thereby weakly transmitting the normal viscous stress to the surface. At early ages, both the geoid and the topography are slightly larger than at older ages, increasing with increasing activation energy, and decreasing to a nearly constant value at about 60 Ma. The higher values at early ages can be explained by the initially large normal viscous stresses in a thin thermal boundary layer. As time increases, the thermal boundary layer thickens, the material in the boundary layer becomes more viscous, and the velocity gradients decrease. The corresponding admittance for case 1 is given in Figure 29. Except for the lowest activation energy calculation, the admittance remains nearly constant around 30 m/km, increasing slightly with increasing activation energy. This value of the admittance is identical with that for uncompensated topography with a wavelength of 2000 km. The basic reason for this is that the low-density compensating mass arising from the thermal perturbation is negligibly small for the time scale of interest. Although the thermal perturbation increases with time as in Figure 23, the growth rate decreases with increasing activation energy, and cannot therefore grow fast enough to compensate the topography. By using Eq. (2) in the long-wavelength limit, an effective depth of compensation can be obtained that will satisfy the observed value of between 6 and 8 m/km for the admittance. The effective depth of compensation ranges from about 58 to 77 km. Relative to the thickness of the layer, these are shallow depths. The thermal perturbation is therefore localized properly, that is, at shallow depth. However, its magnitude is too low, as reflected in the value of the admittance.

For the lowest activation energy calculation, the admittance decreases with time from about 27 m/km to about 17 m/km because the thermal perturbation, which acts to diminish the total geoid, can grow at a faster rate due to the low viscosity of the mechanical lid. However, the admittance is still too

large.

The case of cooling from above with relatively low activation energies clearly cannot satisfactorily predict the observables. The location of the thermal perturbation is roughly correct, however, its magnitude is too low.

Case 2a

In an attempt to increase the magnitude of the thermal perturbation in the time frame of interest (i.e., 30 to 90 Ma), heating from below was added to the model. To make the model more realistic, a low viscosity zone (asthenosphere) with a temperature of 1350°C extending to an initial depth of 200 km, was also incorporated into the model. Also, the mechanical behavior of the lithosphere has been taken into account by using an activation energy of 526 kJ/mol, and a cut-off temperature of 950°C. These conditions apply to both cases 2a and 2b.

In case 2a, the lower boundary of the fluid layer was maintained at a constant temperature of 1450°C, while the core was at an initial temperature of 1300°C. The reference viscosity was 10^{22} Poise at the core temperature. Figure 30 shows the mean temperature scaled by the lower boundary temperature. The time sequence is the same as in the previous profiles. It can be seen that both the cold and the hot thermal boundary layers increase with time. Also, the higher temperature at the LVZ gradually diminishes, and nearly disappears at a dimensionless time of 0.005 due to the large heat flux out of that region. This profile is reflected in the viscosity contrast (Figure 31). The viscosity in the hot thermal boundary layer is lower by about one order of magnitude than the viscosity in the cell core, whereas the viscosity in the LVZ is about one-third that in the cell core at early ages. On the other hand, the viscosity increases rapidly across the cold thermal boundary layer to a value five orders of magnitude higher than that in the cell core. Note that the mechanical lid follows the growth of the cold thermal boundary layer (it is simply the downward migration of the 950°C isotherm). The thermal perturbation (Figure 32) grows rapidly in the hot thermal boundary layer because the viscosity is low, and migrates upward with the growing boundary layer. The existence of the hotter LVZ changes the character of the thermal perturbation there because, as the LVZ cools, heat is transferred towards the surface and towards the cooler cell core, and hence the thermal perturbation is negative there (i.e., the material is cooler than the surroundings). Its growth, however, is slow because the viscosity contrast there is low. In the steady-state case, which has not been considered in this study, the negative thermal perturbation changes sign, increases in magnitude to roughly the magnitude of the lower perturbation, and resides just below the cold thermal boundary layer (personal communication, Dr. Peter Olson). The velocity components (Figures 33-34) increase rapidly with time in the low viscosity fluid in the hot thermal boundary layer. It is clear that mildly vigorous convection is occurring in this case, as can be seen from the vertical component of the velocity. The magnitude of the dimensionless vertical velocity represents the Peclet number, i.e., the ratio of the convective heat loss to the conductive heat loss through the fluid layer.

The topography as a function of age for case 2a appears in Figure 35. It can be seen to increase with age because the convection becomes more vigorous with time, thereby increasing the normal viscous stress which deforms the surface. In Figure 36, the geoid components are shown as a function of age. The thermal contribution to the geoid (dashed line) increases because the thermal perturbation increases with time, but its magnitude is low because the thermal perturbation is buried deep in the fluid layer. The total geoid (solid line) is therefore primarily due to the upper-deformation contribution (dotted line). The admittance is shown in Figure 37. The admittance again has a high value of about 30 m/km for all ages considered. Unlike the thermal perturbation in case 1 which was located properly but of small amplitude, the thermal perturbation in case 2a has a large amplitude but cannot penetrate close to the upper boundary in the time scale considered. To see whether the thermal perturbation could penetrate across the layer in a shorter time scale, the viscosity throughout the fluid layer was reduced by a factor of 10, and the temperature of the lower boundary was raised to 1500°C.

This is case 2b.

Case 2b

The mean temperature and viscosity contrast profiles for case 2b are shown in Figures 38-39 for the ages of 28 Ma (dotted line), 58 Ma (dashed), and 88 Ma (dot-dash). These profiles depart significantly from their counterparts in case 2a. The hot thermal boundary layer is thin because of the high heat flux into the layer from the lower boundary. Because the viscosity in the layer is lower by a factor of 10 everywhere relative to case 2a, the larger fluid motions (Figures 41-42) convect heat effectively across the layer, and the mean temperature in the core of the cell actually increases with time (Figure 38) with a corresponding decrease in the viscosity (Figure 39). The thermal perturbation in this case (Figure 40) slowly rises with time to below the lithosphere, and the thermal contribution to the geoid (dashed line, Figure 43) also increases in magnitude because the thermal anomaly is closer to the surface. However, its increase is not enough to greatly reduce the large value of the total geoid anomaly (solid line, Figure 43). The large convective velocities result in a large normal viscous stress which greatly deforms the surface (Figure 44), and hence the total geoid anomaly is dominated by the upper-deformation contribution (dotted line, Figure 43). The admittance is shown in Figure 45. It is again large (about 30 m/km) and reflects an uncompensated state of the topography because the thermal perturbation is too small, relative to the effect of the surface deformation.

The case of heating the fluid layer from below with the viscosity everywhere lower by a factor of 10 results in very vigorous upper-mantle convection. The upper surface deformation and the total geoid anomaly are also large as a consequence of such vigorous convection. Although the thermal perturbation does develop close to the surface, as is desired to compensate the topography and thus lower the admittance, its growth rate is not large enough to have a very significant effect on reducing the total geoid anomaly. Vigorous convection beneath the Pacific plate must therefore be ruled out.

Case 3

It has already been established here that the thermal perturbation must be shallow relative to the thickness of the layer, and must be of a large enough amplitude to be able to lower the value of the total geoid, and hence lower the admittance. By assuming *a priori* that there is a significant initial thermal perturbation at a shallow depth, the total geoid anomaly, topography, and admittance were calculated and contoured by varying the two parameters: amplitude and depth extent. It is not unreasonable to assume this condition in light of *Woodhouse & Dziewonski's* [1984] seismic tomographic evidence of anomalously low wave velocities below the East Pacific Rise, which can be attributed to anomalously high temperatures. This is case 3.

In case 3, the fluid layer was cooled from above, with the lower boundary held at a temperature of 1300°C. The mechanical properties of the lithosphere were taken into account by using an activation energy of 526 kJ/mol, as well as retaining the LVZ. The resulting geoid anomaly, topography, and admittance for this case are shown in Figures 46-48 at an age of about 60 Ma. The hatched areas in Figures 46-47 correspond to the range of the observed values of geoid anomaly and topography, respectively. There is a trade-off between the initial amplitude of the thermal perturbation and the initial maximum depth extent. If the initial amplitude is large, the perturbation need not extend very deep. On the other hand, if the initial amplitude is small, the perturbation must have a wider vertical extent to produce the same anomaly. Figure 48 shows the admittance in this parameter space. The hatched area corresponds to those combinations of parameters which result in acceptable solutions. That is, those solutions in the hatched area satisfy simultaneously the observed geoid anomaly, topography, and admittance. Figure 48 shows that the thermal perturbation must be shallow (between about 100 and 120 km in depth), and with an amplitude between 65°C and 100°C. Figures 49-53 show the evolution of the temperature and velocity fields for a thermal perturbation with an initial depth extent of 120 km, and an initial amplitude of 78°C. The thermal perturbation (Figure 51) decays

gradually with time. This is the case for all combinations of parameters in the hatched area in Figure 48. The fluid flows in response to this decaying perturbation, and as can be seen in Figures 52-53, the flow also decays with time, and is confined to the low viscosity zone just below the lithosphere. The geoid anomaly, topography, and admittance for this case appear in Figures 54-56, respectively. Because the thermal perturbation decays with time, the fluid flow also decays with time, as well as the resulting geoid anomaly and topography. The large values of the calculations at young ages seem to be an artifact of the numerical model which could not be controlled.

The results of case 3 show that a shallow transient thermal perturbation can satisfactorily explain the observables in the central Pacific. The thermal perturbation, perhaps originating deep in the mantle, could be brought to the surface as a thermal pulse introduced at the ridge, which gradually decays and eventually vanishes. However, the finite life-time of the Pacific plate prevents verification of this idea at much later times. It takes about 400 Ma for a thermal perturbation to be conducted across a lithosphere 100 km thick.

CONCLUSIONS

The geophysical constraints imposed by the intermediate-wavelength geoid anomaly, sea-floor topography, and admittance in the central Pacific suggest that the thermal perturbation responsible for these anomalies must be situated at a shallow depth compared with the thickness of the fluid layer. The results obtained here indicate that the thermal perturbation is sub-lithospheric, lying at a depth of between 100 and 120 km. *McKenzie et al.* [1974] and *Parsons & Daly* [1983] have obtained reasonable agreements between predictions and observations by using a constant-viscosity fluid layer. The reason for these agreements is that in an isoviscous fluid layer the heat from the interior can be transported to a depth close to the upper boundary because of a lack of inhibition from a highly viscous lid. In this case, the thermal perturbation, responsible for the deformation of the sea-floor and its compensation, can fully develop at shallow depths, and in short time scales. However, no account has been taken for the development of a rigid lid at the cold thermal boundary layer. In fact, the existence of a quasi-rigid mechanical lid completely dictates the results, prohibiting any possible development of the thermal perturbation in the vicinity of the lithosphere, and in the proper time scale. *McKenzie* [1977] has found that the admittance in a highly variable-viscosity fluid is about one order of magnitude higher than it is for an isoviscous fluid. Also, he finds that the predicted values for the admittance in his calculations are compatible with the observations of *Sclater et al.* [1975] for the North Atlantic, and *Watts* [1976] for the central Pacific if a sinusoidal temperature variation is imposed at the top of a low-viscosity layer overlying a higher viscosity half-space. This supports our conclusion that shallow thermal variations are required to explain the observed anomalies. There appears to be no way in which the observables and mechanical behavior of the lithosphere can be simultaneously predicted by neglecting the temperature dependence of the viscosity. Hence, the main conclusion emerging from this study is that organized small-scale convection in the upper-mantle with a dominant wavelength of about 2000 km cannot possibly exist if the temperature-dependent nature of the viscosity structure is considered.

Acknowledgements. This work has benefited from many discussions with Peter Olson while one of the authors (JHH) was doing doctoral work at Johns Hopkins. We would like to thank J.G. Marsh of the NASA Goddard Space Flight Center for providing the SEASAT data. This study was supported by NASA grant NAG5-32 to The Johns Hopkins University.

APPENDIX A: GOVERNING EQUATIONS

The relevant equations are those expressing the conservation of mass, momentum, and energy. If the flow is considered to be incompressible, the equation of continuity of mass is

$$\nabla \cdot \mathbf{u} = 0 \tag{A1}$$

where $\mathbf{u} = (u,w)$ is the two-dimensional velocity vector in a vertical plane (x,z) parallel to the ridge axis.

The equations of motion expressing conservation of momentum in a Boussinesq, infinite Prandtl number fluid are

$$0 = -\nabla P' + \Delta\rho \mathbf{g} + \nabla \cdot \tau \tag{A2}$$

where P' is the pressure relative to the lithostatic pressure arising from the flow, $\Delta\rho$ is the density anomaly arising from the thermal variations, $\mathbf{g}$ is the acceleration-of-gravity vector, and τ is the viscous stress tensor. The second term on the right-hand side of Eq. (A2) is the buoyancy force per unit volume which drives the convection. Using a linear equation of state, the buoyancy term becomes $-\rho_o \alpha g(T-\overline{T})$, where ρ_o is the density at temperature $\overline{T}$, and α is the coefficient of thermal expansion. The third term on the right side of Eq. (A2) is the viscous force per unit volume which tends to retard the flow. Assuming a Newtonian rheology, the viscous stress tensor can be written in indicial notation as

$$\tau_{ij} = \eta\left(\frac{\partial u_i}{\partial x_j} + \frac{\partial u_j}{\partial x_i}\right) \tag{A3}$$

where i and j can be either x or z, and η is the dynamic viscosity which is here a function of temperature. Taking the curl of Eq. (A2) to eliminate the pressure term results in the vorticity equation given by

$$\left(\frac{\partial^2}{\partial z^2} - \frac{\partial^2}{\partial x^2}\right)\left[\eta\left(\frac{\partial u}{\partial z} + \frac{\partial w}{\partial x}\right)\right] - 4\frac{\partial^2}{\partial x \partial z}\left(\eta\frac{\partial w}{\partial z}\right) = \rho_o \alpha g \frac{\partial T}{\partial x} \qquad \text{(A4)}$$

Conservation of energy is expressed by the heat transport equation. Neglecting internal heat generation and viscous dissipation of mechanical work, the energy equation is

$$\frac{\partial T}{\partial t} + \mathbf{u} \cdot \nabla T = \kappa \nabla^2 T \qquad \text{(A5)}$$

where T is the temperature and κ is the thermal diffusivity. The second term on the left-hand side of Eq. (A5) is the convective transport of heat, while the right-hand side contains the diffusion term.

The equations of conservation of mass, momentum, and energy cannot be solved analytically because of the non-linearities introduced by the variable viscosity and the finite-amplitude convective velocities. They can, however, be solved numerically by the use of finite-difference schemes, subject to suitable boundary and initial conditions. Even then, the computation is likely to take a large amount of CPU time. A major simplification can be achieved by using the single-mode, mean-field approximation to the two-dimensional convection problem at high Rayleigh and Prandtl numbers. This approximation has been used extensively in the past to study stellar convection [e.g., *Toomre et al.*, 1982], and has also been applied to problems in mantle convection for constant viscosity by *Olson* [1981] and for variable viscosity by *Yuen & Fleitout* [1984], among others. *Quareni et al.* [1985] have compared mean-field and two-dimensional solutions and have found that the two formulations yield identical solutions for Rayleigh numbers close to the critical value. Increasing the Rayleigh number increases the difference between the two solutions, but the general trends of the flow are still predictable.

The mean field approximation consists of expressing the full temperature field in terms of a mean temperature, $\overline{T}$, and a fluctuating temperature, θ, being expanded in terms of a Fourier series along the horizontal coordinate x. Keeping only the first term in the expansion results in the single-mode expression of the mean-field approximation. The temperature can thus be written as

$$T(x,z,t) = \overline{T}(z,t) + \theta(z,t)\cos(kx) \qquad \text{(A6)}$$

where k is the wavenumber of the single mode. Note that the temperature dependence of viscosity can be simplified by assuming that the viscosity is a function only of the mean temperature profile.

The velocity field is also expanded in a Fourier series, and with a single-mode representation the equations of motion can be linearized. Let the vertical velocity, shear stress, horizontal velocity, and net normal stress be given, respectively, by

$$w(x,z,t) = A_1(z,t)\cos(kx) \tag{A7a}$$

$$\tau_{xz}(x,z,t) = A_2(z,t)\sin(kx) \tag{A7b}$$

$$u(x,z,t) = A_3(z,t)\sin(kx) \tag{A7c}$$

$$\sigma_{xx}(x,z,t) = (A_4(z,t)/k)\cos(kx) \tag{A7d}$$

The A's are the variable amplitudes of the periodic perturbations. By substituting Eqs. (A7) into the equations of continuity and motion, the following system of ordinary differential equations results

$$\frac{d}{dz}\begin{bmatrix} A_1 \\ A_2 \\ A_3 \\ A_4 \end{bmatrix} = \begin{bmatrix} 0 & 0 & -k & 0 \\ 0 & 0 & 4k^2\eta & 1 \\ k & 1/\eta & 0 & 0 \\ 0 & -k^2 & 0 & 0 \end{bmatrix}\begin{bmatrix} A_1 \\ A_2 \\ A_3 \\ A_4 \end{bmatrix} + \begin{bmatrix} 0 \\ 0 \\ 0 \\ -\rho_o \alpha g k \theta \end{bmatrix} \tag{A8}$$

Note that in the above system of equations no derivatives of the viscosity function appear, thus allowing for a completely general treatment of viscosity variations in the vertical. In the system Eq. (A8), the variables A_1, A_2, A_3, and A_4 are explicit functions of the vertical coordinate, and are implicit functions of time through the viscosity and the perturbation temperature.

Substitution of Eqs. (A6), (A7a), and (A7c) into the heat transport equation (Eq.(A5)) results in two equations for the mean temperature and the fluctuating temperature, given, respectively, by

$$\frac{\partial \overline{T}}{\partial t} + \frac{1}{2}\frac{\partial}{\partial z}\left(A_1\theta\right) = \kappa\frac{\partial^2 \overline{T}}{\partial z^2} \tag{A9a}$$

$$\frac{\partial \theta}{\partial t} + A_1\frac{\partial \overline{T}}{\partial z} = \kappa\left(\frac{\partial^2 \theta}{\partial z^2} - k^2\theta\right) \tag{A9b}$$

The boundaries of the layer are assumed to be isothermal and stress-free, i.e.,

$$\overline{T} = T_o \quad at\ z = 0, \quad t \geq 0 \tag{A10a}$$

$$\overline{T} = T_1 \quad at\ z = d, \quad t > 0 \tag{A10b}$$

$$\theta = 0 \quad at\ z = 0, d; \quad t \geq 0 \tag{A10c}$$

where $T_o > T_1$, and

$$w = \tau_{xz} = 0 \quad at\ z = 0, d; \quad t \geq 0 \tag{A11a}$$

$$A_1 = A_2 = 0 \quad at\ z = 0, d; \quad t \geq 0 \tag{A11b}$$

Eqs. (A11) are conditions that allow for deformation of the boundaries.

To completely specify the problem, the initial conditions must be given. It is assumed that the fluid is initially at a constant uniform temperature T_o. At time $t = 0$, the upper boundary is set to $T_1 = 0°C$, as would be the case along a ridge crest. In an undisturbed layer of fluid $A_1 = \theta = 0$, and heat is transferred purely by conduction. The solution to Eq. (A9a) in this case is given by the error function solution

$$\overline{T}(z,t) = T_o erf\left[\frac{y}{2\sqrt{\kappa t}}\right] \tag{A12}$$

where $y = d - z$, d is the layer depth. However, to induce the growth of only one mode of circulation, a periodic temperature perturbation with a wavelength equal to twice the layer depth and with an amplitude of $1°C$ is used, i.e.,

$$\theta(z, 0) = \theta_o \sin\left(\frac{\pi z}{d}\right) \tag{A13}$$

where $\theta_o = 1°C$.

The equations governing the fluid flow and the transport of heat can be non-dimensionalized by introducing the following dimensionless variables

$$z' = z/d \tag{A14a}$$

$$k' = kd \tag{A14b}$$

$$t' = \kappa t/d^2 \tag{A14c}$$

$$(T',\theta') = (T,\theta)/\Delta T,\ \Delta T = T_o - T_1 \tag{A14d}$$

$$\eta' = \frac{\eta}{\eta_o},\ \eta_o = \eta(T_o) \tag{A14e}$$

Dropping the primes for clarity, the non-dimensional form of Eq. (A8) is

$$\frac{d}{dz}\begin{bmatrix} A_1 \\ A_2 \\ A_3 \\ A_4 \end{bmatrix} = \begin{bmatrix} 0 & 0 & -k & 0 \\ 0 & 0 & 4k^2\eta & 1 \\ k & 1/\eta & 0 & 0 \\ 0 & -k^2 & 0 & 0 \end{bmatrix}\begin{bmatrix} A_1 \\ A_2 \\ A_3 \\ A_4 \end{bmatrix} + \begin{bmatrix} 0 \\ 0 \\ 0 \\ -Ra\,k\,\theta \end{bmatrix} \tag{A15}$$

where $Ra = \rho_o \alpha g \Delta T d^3/\eta_o \kappa$ is the Rayleigh number based on the temperature drop across the layer, and the viscosity is the reference viscosity.

The mean-temperature and fluctuating-temperature equations in dimensionless form are, respectively,

$$\frac{\partial \overline{T}}{\partial t} + \frac{1}{2}\frac{\partial}{\partial z}\left(A_1\theta\right) = \frac{\partial^2 \overline{T}}{\partial z^2} \tag{A16a}$$

$$\frac{\partial \theta}{\partial t} + A_1\frac{\partial \overline{T}}{\partial z} = \frac{\partial^2 \theta}{\partial z^2} - k^2\theta \tag{A16b}$$

Accordingly, the boundary conditions are

$$\overline{T} = 1 \quad at\ z = 0,\ \ t \geq 0 \tag{A17a}$$

$$\overline{T} = 0 \quad at\ z = 1,\ \ t > 0 \tag{A17b}$$

$$\theta = 0 \quad at\ z = 0,\ 1;\quad t \geq 0 \tag{A17c}$$

$$A_1 = A_2 = 0 \quad at\ z = 0,\ 1;\quad t \geq 0 \tag{A17d}$$

and the initial conditions are

$$\overline{T} = 1 \quad at\ t = 0,\quad 0 \leq z < 1 \tag{A18a}$$

$$\overline{T} = 0 \quad at\ t = 0,\quad z = 1 \tag{A18b}$$

$$\theta = (\theta_o/\Delta T)\sin(\pi z) \quad at\ t = 0,\quad 0 \leq z \leq 1 \tag{A18c}$$

APPENDIX B: DERIVATION OF EXPRESSIONS FOR GEOID AND TOPOGRAPHY

In this appendix, the anomalous geoid and topography will be derived and numerically calculated in terms of the quantities which characterize the flow and heat transport in a fluid layer of temperature-dependent viscosity.

Consider the circulation in Figure 20. The flow is physically confined to remain within the upper and lower boundaries. But, because the viscous shear stress is assumed to vanish at the boundaries, they are free to deform. To obtain the deformation of the boundaries, the equilibrium condition that the net normal stress vanish there must be satisfied. That is to say,

$$\sigma_{zz}(x) = 0 \tag{B1}$$

But, by definition,

$$\sigma_{zz}(x) = -P(x) + \tau_{zz}(x) \tag{B2}$$

where $P(x)$ is the total pressure, and $\tau_{zz}(x)$ is the normal viscous stress. But, the total pressure can be expressed as the sum of a hydrostatic term, P_o, and a perturbation term, P', which arises from the flow. Hence,

$$P(x) = P_o(x) + P'(x) \tag{B3}$$

From the choice of the z-axis, the hydrostatic pressure term can be written as

$$P_o(x) = -\Delta\rho g_o w(x) \tag{B4}$$

where $w(x)$ is the boundary deformation, and $\Delta\rho$ is the corresponding density contrast across the boundary. The condition (B1) now becomes

$$\Delta\rho g_o w(x) = P'(x) - \tau_{xx}(x) \tag{B5}$$

The perturbation pressure can be obtained from the x-component of the equation of motion. By recalling the single-mode representations, Eqs. (A7), the expression for the amplitude of the boundary deformation becomes

$$w_o = \left.\frac{4\eta k A_3}{\Delta\rho g_o}\right|_{z'} \tag{B6}$$

where η and A_3 are evaluated at z' ($z' = 0$ at the lower boundary and $z' = 1$ at the upper boundary), with the appropriate value for the density contrast.

The deformation of the upper boundary is

$$w_o = \frac{4\eta(1) k A_3(1)}{(\rho_m - \rho_w) g_o} \tag{B7}$$

Model predictions of topography can then be made with Eq. (B7).

It now remains to derive an expression for the total geoid anomaly at the sea surface arising from the fluid flow. Recall that the total geoid anomaly is the resultant of three contributions: i) the effect due to the upper boundary deformation, ii) the effect due to the lower boundary deformation, and iii) the effect due to the internal density anomalies arising from the thermal variations within the layer of fluid.

(i) The amplitude of the geoid anomaly due to the upper boundary deformation is [*McKenzie & Bowin*, 1976]

$$N_{wp}(z = s + d) = \frac{2\pi\Gamma(\rho_m - \rho_w) w_o}{g_o k} e^{-ks} \tag{B8}$$

where w_o is given by Eq. (B7) and, again, all terms are as defined before. Note that this is a positive contribution to the geoid.

(ii) The amplitude of the geoid anomaly due to the lower boundary deformation is

$$N_{lo}(z = s + d) = \frac{8\pi\Gamma}{g_o^2}\eta(0)A_3(0)e^{+k(s+d)} \tag{B9}$$

Note that the density contrast across the lower boundary does not appear in Eq. (B9). However, for gravitational stability to occur at the lower boundary, the material below must be denser than the one above. And since the deformation of the lower boundary is positive, the geoid contribution is also positive.

(iii) The amplitude of the geoid anomaly produced by the thermal variations within the layer is obtained by first calculating the gravitational potential at a point above a rising limb of a convection cell. This field point is chosen because this is where the anomaly reaches an extremum (in this case, a minimum).

The general expression for the anomalous gravitational potential due to distributed two-dimensional density anomalies is

$$\Delta U(x,z) = \Gamma \int_{x'} \int_{z'} \frac{\Delta\rho(x',z')dx'dz'}{\sqrt{(x-x')^2 + (z-z')^2}} \tag{B10}$$

where the primed variables are the source variables, and the unprimed variables are the field variables. The density anomaly due to thermal variations is

$$\Delta\rho(x',z') = -\rho_m\alpha\Delta T(x',z') \tag{B11}$$

and

$$\Delta T(x',z') = T(x',z') - \overline{T}(z') = \theta(z')\cos(kx') \tag{B12}$$

Now, by virtue of the fact that the temperature perturbation is periodic in the horizontal coordinate, the integration over x' can be extended from $-\infty$ to $+\infty$. Evaluating the potential at the field point $(x,z) = (0, s+d)$ and noting that the cosine function is an even function, Eq. (B10) becomes

$$\Delta U(0,s+d) = -2\rho_m \alpha \Gamma \int_o^\infty \int_o^d \frac{\theta(z')\cos(kx')dx'dz'}{\sqrt{x'^2 + (s+d-z')^2}} \tag{B13}$$

But, the integral over x' is nothing more than the Fourier cosine transform of one over the denominator at a fixed z'. By using Brun's formula to relate the potential to the geoid, the expression to evaluate for the thermal contribution to the geoid anomaly is

$$N_\theta(0,s+d) = \frac{-2\rho_m \alpha \Gamma}{g_o} \int_o^d K_o(kr)\theta(z')dz' \tag{B14}$$

where $K_o(kr)$ is the modified Bessel function of the second kind and zero order, $r = s+d-z'$, and k is the wavenumber. (Note that this is a negative contribution to the geoid). The function K_o decreases rapidly with increasing argument.

This expression can be numerically integrated by using the trapezoidal rule on the calculated fluctuating temperature profile at a given time, and by making a 6^{th} order polynomial approximation of the Bessel function. The total geoid anomaly is then

$$N_T = N_{sp} + N_{lo} + N_\theta \tag{B15}$$

References

Bloomfield, P., *Fourier analysis of time series: An introduction*, John Wiley & Sons. Inc., New York, 1976.

Buck, W.R., and E.M. Parmentier, Convection beneath young oceanic lithosphere: Implications for thermal structure and gravity, *J. Geophys. Res., 91,* 1961-1974, 1986.

Cathles, L.M., *The viscosity of the earth's mantle,* Princeton Univ. Press, Princeton, N.J., 1975.

Cazenave, A., B. Lago, and K. Dominh, Geoid anomalies over the northeast Pacific fracture zones from satellite altimeter data, *Geophys. J.R. Astr. Soc., 69,* 15-31, 1982.

Cazenave, A., B. Lago, and K. Dominh, Thermal parameters of the oceanic lithosphere estimated from geoid height data, *J. Geophys. Res., 88,* 1105-1118, 1983.

Chapman, M.E., and M. Talwani, Geoid anomalies over deep sea trenches, *Geophys. J.R. Astr. Soc., 68,* 349-369, 1982.

Chase, C.G., Subduction, the geoid, and lower mantle convection, *Nature, 282,* 464-468, 1979.

Cochran, J.R., An analysis of isostasy in the world's oceans. 2. Mid-ocean ridge crests, *J. Geophys. Res., 84,* 4713-4729, 1979.

Crough, S.T., and D.M. Jurdy, Subducted lithosphere, hotspots, and the geoid, *Earth Planet. Sci. Lett., 48,* 15-22, 1980.

Davies, G.F., Whole-mantle convection and plate tectonics, *Geophys. J.R. Astr. Soc., 49,* 459-486, 1977.

Detrick, R.S., An analysis of geoid anomalies across the Mendocino fracture zone: Implications for thermal models of the lithosphere, *J. Geophys. Res., 86,* 11751-11762, 1981.

Detrick, R.S., and A.B. Watts, An analysis of isostasy in the world's oceans. 3. Aseismic ridges, *J. Geophys. Res., 84,* 3637-3653, 1979.

Dorman, L.M., and B.T.R. Lewis, Experimental isostasy. 1. Theory of the determination of the earth's isostatic response to a concentrated load, *J. Geophys. Res., 75,* 3357-3365, 1970.

Dorman, L.M., and B.T.R. Lewis, Experimental isostasy. 3. Inversion of the isostatic Green function and lateral density changes, *J. Geophys. Res., 77,* 3068-3077, 1972.

Elsasser, W.M., P. Olson, and B.D. Marsh, The depth of mantle convection, *J. Geophys. Res., 84,* 147-155, 1979.

Grow, J.A., and C.O. Bowin, Evidence for high density crust and mantle beneath the Chile trench due to the descending lithosphere, *J. Geophys. Res., 80,* 1449-1458, 1975.

Hager, B.H., Subducted slabs and the geoid: Constraints on mantle rheology and flow, *J. Geophys. Res., 89,* 6003-6015, 1984.

Haxby, W.F., and D.L. Turcotte, On isostatic geoid anomalies, *J. Geophys. Res., 83,* 5473-5478, 1978.

Haxby, W.F., D.L. Turcotte, and J.M. Bird, Thermal and mechanical evolution of the Michigan basin, *Tectonophys., 36,* 57-75, 1976.

Haxby, W.F., and J.K. Weissel, Evidence for small-scale mantle convection from SEASAT altimeter data, *J. Geophys. Res., 91,* 3507-3520, 1986.

Heestand, R.L., and S.T. Crough, The effect of hot spots on the oceanic depth-age relation, *J. Geophys. Res., 86,* 6107-6114, 1981.

Hinojosa, J.H., On the state of isostasy in the central Pacific: Static and dynamic compensation mechanisms, PhD dissertation, The Johns Hopkins University, 276 pp., 1986.

Jaupart, C., and B. Parsons, Convective instabilities in a variable viscosity fluid cooled from above, *Phys. Earth Planet. Inter., 39,* 14-32, 1985.

Lerch, F.J., J.G. Marsh, S.M. Klosko, and R.G. Williamson, Gravity model improvement for SEASAT, *J. Geophys. Res., 87,* 3281-3296, 1982.

Marsh, B.D., and J.G. Marsh, On global gravity anomalies and two-scale mantle convection, *J. Geophys. Res., 81,* 5267-5280, 1976.

Marsh, J.G., and T.V. Martin, The SEASAT altimeter mean sea surface model, *J. Geophys. Res., 87,* 3269-3280, 1987.

Marsh, J.G., A.C. Brenner, B.D. Beckley, and T.V. Martin, Global mean sea surface based upon the SEASAT altimeter data, *J. Geophys. Res., 91,* 3501-3506, 1986.

McAdoo, D.C., Geoid anomalies in the vicinity of subduction zones, *J. Geophys. Res., 86,* 6073-6090, 1981.

McAdoo, D.C., J.G. Caldwell, and D.L. Turcotte, On the elastic-perfectly plastic bending of the lithosphere under generalized loading with application to the Kuril Trench, *Geophys. J.R. Astr. Soc., 54,* 11-26, 1978.

McKenzie, D., Surface deformation, gravity anomalies and convection, *Geophys. J.R. Astr. Soc., 48,* 211-238, 1977.

McKenzie, D., and C. Bowin, The relationship between bathymetry and gravity in the Atlantic Ocean, *J. Geophys. Res., 81,* 1903-1915, 1976.

McKenzie, D., and N.O. Weiss, Speculations on the thermal and tectonic history of the earth, *Geophys. J.R. Astr. Soc., 42,* 131-174, 1975.

McKenzie, D.P., J.M. Roberts, and N.O. Weiss, Convection in the earth's mantle: Towards a numerical simulation, *J. Fluid Mech., 62,* 465-538, 1974.

McKenzie, D., A.B. Watts, B. Parsons, and M. Roufosse, Planform of mantle convection beneath the Pacific Ocean, *Nature, 288,* 442-446, 1980.

McNutt, M., Compensation of oceanic topography: An application of the response function technique to the Surveyor area, *J. Geophys. Res., 84,* 7589-7598, 1979.

McNutt, M.K., Lithospheric flexure and thermal anomalies, *J. Geophys. Res., 89,* 11180-11194, 1984.

McNutt, M.K., and H.W. Menard, Lithospheric flexure and uplifted atolls, *J. Geophys. Res., 83,* 1206-1212, 1978.

McNutt, M.K., and R.L. Parker, Isostasy in Australia and the evolution of the compensation mechanism, *Science, 199,* 773-775, 1978.

Menard, H.W., Depth anomalies and the bobbing motion of drifting islands, *J. Geophys. Res., 78,* 5128-5137, 1973.

Olson, P., Mantle convection with spherical effects, *J. Geophys. Res., 86,* 4881-4890, 1981.

Parker, R.L., and D.W. Oldenburg, Thermal model of ocean ridges, *Nature Phys. Sci., 242,* 137-139, 1973.

Parsons, B., and S. Daly, The relationship between surface topography, gravity anomalies, and temperature structure of convection, *J. Geophys. Res., 88,* 1129-1144, 1983.

Parsons, B., and D.P. McKenzie, Mantle convection and the thermal structure of the plates, *J. Geophys. Res., 83,* 4485-4496, 1978.

Parsons, B., and P. Molnar, The origin of outer topographic rises associated with trenches, *Geophys. J.R. Astr. Soc., 45,* 707-712, 1976.

Parsons, B., and J.G. Sclater, An analysis of the variation of ocean floor bathymetry and heat flow with age, *J. Geophys. Res., 82,* 803-827, 1977.

Quareni, F., D.A. Yuen, G. Sewell, U.R. Christensen, High Rayleigh number convection with strongly variable viscosity: A comparison between mean field and two-dimensional solutions, *J. Geophys. Res., 90,* 12633-12644, 1985.

Richards, M.A., and B.H. Hager, Geoid anomalies in a dynamic earth, *J. Geophys. Res., 89,* 5987-6002, 1984.

Richter, F.M., Dynamical models for sea floor spreading, *Rev. Geophys. Space Phys., 11,* 223-287, 1973.

Richter, F.M., and S.F. Daly, Convection models having a multiplicity of large horizontal scales, *J. Geophys. Res., 83,* 4951-4956, 1978.

Richter, F.M., and B. Parsons, On the interaction of two scales of convection in the mantle, *J. Geophys. Res., 80,* 2529-2541, 1975.

Runcorn, S.K., Satellite gravity measurements and convection in the mantle, *Nature, 200,* 628-630, 1963.

Runcorn, S.K., Satellite gravity measurements and a laminar viscous flow model of the earth's mantle, *J. Geophys. Res., 69,* 4389-4394, 1964.

Sandwell, D.T., and M.L. Renkin, Compensation of swells and plateaus in the North Pacific: No direct evidence for mantle convection, *J. Geophys. Res., 93,* 2775-2783, 1988.

Sandwell, D.T., and G. Schubert, Geoid height-age relation from SEASAT altimeter profiles across the Mendocino fracture zone, *J. Geophys. Res., 87,* 3949-3958, 1982.

Schubert, G., C. Froidevaux, and D.A. Yuen, Oceanic lithosphere and asthenosphere: Thermal and mechanical structure, *J. Geophys. Res., 81,* 3525-3540, 1976.

Sclater, J.G., and G. Francheteau, The implication of terrestrial heat flow observations on current tectonic and geochemical models of the crust and upper mantle of the earth, *Geophys. J.R. Astr. Soc., 20,* 509-537, 1970.

Sclater, J.G., L.A. Lawver, and B. Parsons, Comparison of long-wavelength residual elevation and free-air gravity anomalies in the North Atlantic and possible implications for the thickness of the lithospheric plate, *J. Geophys. Res., 80,* 1031-1052, 1975.

Sleep, N.H., and N.S. Snell, Thermal contraction and flexure of mid-continent and Atlantic marginal basins, *Geophys. J.R. Astr. Soc., 45,* 125-154, 1976.

Toomre, J., D.O. Gough, and E.A. Spiegel, Time-dependent solutions of multimode convection equations, *J. Fluid Mech., 125,* 99-122, 1982.

Turcotte, D.L., and E.R. Oxburgh, Finite amplitude convective cells and continental drift, *J. Fluid Mech., 28,* 29-42, 1967.

Turcotte, D.L., and G. Schubert, *Geodynamics: Applications of continuum physics to geological problems,* John Wiley & Sons, Inc., New York, 1982.

Watts, A.B., Gravity and bathymetry in the Central Pacific Ocean, *J. Geophys. Res., 81* 1533-1576. 1976.

Watts, A.B., On geoid heights derived from GEOS-3 altimeter data along the Hawaiian-Emperor seamont chain, *J. Geophys. Res., 84,* 3817-3826, 1979.

Watts, A.B., An analysis of isostasy in the world's oceans. 1. Hawaiian-Emperor seamount chain, *J. Geophys. Res., 83,* 5989-6004, 1978.

Watts, A.B., and S.F. Daly, Long wavelength gravity and topography anomalies, *Ann. Rev. Earth Planet. Sci., 9,* 415-448, 1981.

Watts, A.B., and M. Talwani, Gravity effect of downgoing lithospheric slabs beneath island arcs, *Geol. Soc. Am. Bull., 86,* 1-4, 1975.

Watts, A.B., J.H. Bodine, and N.M. Ribe, Observations of flexure and the geological evolution of the Pacific Ocean basin, *Nature, 283,* 532-537, 1980.

Watts, A.B., D.P. McKenzie, B. Parsons, and M. Roufousse, The relationship between gravity and bathymetry in the Pacific Ocean, *Geophys. J.R. Astron. Soc., 83,* 263-298, 1985.

Woodhouse, J.H., and A.M. Dziewonski, Mapping the upper mantle: Three dimensional modeling of Earth structure by inversion of seismic waveforms, *J. Geophys, Res., 89,* 5953-5986, 1984.

Yuen, D.A., and L. Fleitout, Stability of the oceanic lithosphere with variable viscosity: An initial value approach, *Phys. Earth Planet. Inter., 34,* 173-185, 1984.

Yuen, D.A., W.R. Peltier, and G. Schubert, On the existence of a second scale of convection in the upper mantle, *Geophys. J.R. Astr. Soc., 65,* 171-190, 1981.

Figure Captions

Fig. 1. The SEASAT geoid relative to a reference ellipsoid defined by a = 6378.137 km and f = 1/298.257 obtained from altimeter measurements. Contour interval = 2 m (Courtesy of J.G. Marsh, NASA, GSFC).

Fig. 2. Elastic thickness as a function of age of the oceanic lithosphere at the time of loading. The data are from *Watts et al.* [1980]. The solid curves are the 300°C and 600°C isotherms based on a cooling plate model (from *Watts & Daly* [1981]).

Fig. 3. The SEASAT geoid anomalies minus the GEM 10B (12,12) geoid field model. Contour interval = 2 m (Courtesy of J.G. Marsh, NASA, GSFC).

Fig. 4. Airy model admittance curves for the values of depth of compensation shown next to each curve.

Fig. 5. Flexure model admittance curves for the values of effective elastic plate thickness shown next to each curve.

Fig. 6. Map showing the location of the study area in the central Pacific Ocean.
Longitude: 205° to 236°
Latitude: -13° to 18°

Fig. 7. Contour map showing the raw bathymetry in the study area. Contour interval = 300 m.

Fig. 8. Contour map showing the age of the sea-floor in the study area. Several major fracture zones are apparent in the map. Contour interval = 10 Ma.

Fig. 9. Contour map showing the sea-floor topography obtained by Gaussian high-pass filtering the bathymetry in the study area. Contour interval = 100 m.

Fig. 10. The observed admittance obtained by taking the ratio of the geoid to the topography in the wavenumber domain. This quantity expresses the geoid anomaly in meters for every kilometer of the sea-floor topography at a given wavelength. The error bars are one-standard-deviation uncertainties.

Fig. 11. Phase spectrum of the observed admittance.

Fig. 12. Coherence spectrum between geoid and topography.

Fig. 13. Comparison of the observed admittance spectrum with flexure model admittance curves for the values of the elastic plate thicknesses shown next to each curve.

Fig. 14. Comparison of the observed admittance spectrum with the Airy model admittance curve corresponding to a depth of compensation of 25 km.

Fig. 15. The resultant geoid field after removing a first degree surface from the full geoid. Contour interval = 2 m.

Fig. 16. The resultant geoid field after removing a second degree surface from the full geoid.

Contour interval = 1 m.

Fig. 17. The resultant geoid field after removing a third degree surface from the full geoid. Contour interval = 1 m.

Fig. 18. The resultant topography field after removing a third degree surface from the bathymetry in Fig. 7. Contour interval = 200 m.

Fig. 19. Scatter plot of the geoid (Fig. 17) and topography (Fig. 18).

Fig. 20. Schematic diagram showing the model of the lithosphere and the underlying upper mantle with single-mode circulation in rolls oriented parallel to the direction of plate motion.

Fig. 21. The mean temperature profile for case 1 in which the fluid layer is cooled from above. The lower-boundary temperature is fixed at 1300°C, the Rayleigh number is 5.85×10^5, the reference viscosity at T = 1300°C is 10^{22} Poise, the activation energy is 51 kJ/mol, and the cut-off temperature is 450°C. The profiles were taken at Fourier times of 0.001 (dotted line), 0.002 (dashed line), 0.003(dot-dash), 0.004 (long dash-dot), 0.005 (dash-dot-dot-dot).

Fig. 22. The viscosity contrast profile for case 1 as described in the caption to Fig. 21.

Fig. 23. The fluctuating temperature profile for case 1 as described in the caption to Fig. 21.

Fig. 24. The horizontal velocity profile for case 1 as described in the caption to Fig. 21.

Fig. 25. The vertical velocity profile for case 1 as described in the caption to Fig. 21.

Fig. 26. The geoid components as a function of age for case 1 as described in the caption to Fig. 21. The open triangles are the calculated values. The solid line is the total geoid anomaly. The dotted line is the upper-boundary-deformation contribution, the dashed line is the thermal contribution, and the dot-dashed line is the lower-boundary-deformation contribution.

Fig. 27. The total geoid anomaly as a function of age for case 1 with different values for the activation energy in kJ/mol: 51 (dotted line), 77 (dashed), 102 (dot-dash), 128 (long dash-dot), and 154 (dash-dot-dot-dot).

Fig. 28. The topography as a function of age for case 1 with the different values for the activation energy as described in the caption to Fig. 27.

Fig. 29. The admittance as a function of age for case 1 with the different values for the activation energy as described in the caption to Fig. 27.

Fig. 30. The mean temperature profile for case 2a in which the fluid layer is heated from below. The temperature of the lower boundary is maintained at 1450°C, the Rayleigh number is 6.53×10^5, the reference viscosity at T = 1300°C is 10^{22} Poise, the activation energy is 526 kJ/mol, the cut-off temperature is 950°C, and the initial LVZ temperature is 1350°C extending to a depth of 200 km.

Fig. 31. The viscosity contrast profile for case 2a as described in the caption to Fig. 30.

Fig. 32. The fluctuating temperature profile for case 2a as described in the caption to Fig. 30.

Fig. 33. The horizontal velocity profile for case 2a as described in the caption to Fig. 30.

Fig. 34. The vertical velocity profile for case 2a as described in the caption to Fig. 30.

Fig. 35. The topography as a function of age for case 2a as described in the caption to Fig. 30.

Fig. 36. The geoid components as a function of age for case 2a as described in the caption to Fig. 30. The solid line is the total geoid anomaly, the dotted line is the upper-boundary-deformation contribution, the dashed line is the thermal contribution, and the dot-dashed line is the lower-boundary-deformation contribution.

Fig. 37. The admittance as a function of age for case 2a as described in the caption to Fig. 30.

Fig. 38. The mean temperature profile for case 2b in which the fluid layer is heated from below. The temperature of the lower boundary is maintained at 1500°C, the Rayleigh number is 6.75×10^6, the reference viscosity at T = 1300°C is 10^{21} Poise, the activation energy is 526 kJ/mol, the cut-off temperature is 950°C, and the initial LVZ temperature is 1350°C extending to a depth of 200 km. The time sequence corresponds to the ages of 28 Ma (dotted line), 58 Ma (dashed), and 88 Ma (dot-dash).

Fig. 39. The viscosity contrast profile for case 2b as described in the caption to Fig. 38.

Fig. 40. The fluctuating temperature profile for case 2b as described in the caption to Fig. 38.

Fig. 41. The horizontal velocity profile for case 2b as described in the caption to Fig. 38.

Fig. 42. The vertical velocity profile for case 2b as described in the caption to Fig. 38.

Fig. 43. The geoid components as a function of age for case 2b as described in the caption to Fig. 38. The solid line is the total geoid anomaly, the dotted line is the upper-boundary-deformation contribution, the dashed line is the themal contribution, and the dot-dashed line is the lower-boundary-deformation contribution.

Fig. 44. The topography as a function of age for case 2b as described in the caption to Fig. 38.

Fig. 45. The admittance as a function of age for case 2b as described in the caption to Fig. 38.

Fig. 46. The parameter space for the predicted geoid anomaly for case 3 in which the fluid layer is cooled from above, the lower boundary temperature is fixed at 1300°C, the Rayleigh number is 5.85×10^5, the mean viscosity at T = 1300°C is 10^{22} Poise, the activation energy is 526 kJ/mol, the cut-off temperature is 950°C, and the initial LVZ temperature is 1350°C extending to a depth of 200 km. The thermal perturbation was initially introduced extending from the surface down to a given depth (horizontal axis) and of a given initial amplitude (vertical axis). The hatched area corresponds to the range of the observed geoid anomaly. Contour interval = 1 m.

Fig. 47. The parameter space for the predicted topography for case 3 as described in the caption to Fig. 46. The hatched area corresponds to the range of the observed topography. Contour interval = 0.05 km.

Fig. 48. The parameter space for the predicted admittance for case 3 as described in the caption to Fig. 46. The hatched area corresponds to the range where the geoid, topography, and admittance

simultaneously satisfy the observations. Contour interval = 1m/km.

Fig. 49. The mean temperature profile for case 3 as described in the caption to Fig. 46 and for the best combination of parameters as inferred from the hatched area on Fig. 48. The initial depth of the thermal perturbation is 120 km, and the initial amplitude is 78°C. The profiles were taken at Fourier times of 0.001 (dotted line). 0.002 (dashed), 0.003 (dot-dash), 0.004 (long dash-dot), and 0.005 (dash-dot-dot-dot).

Fig. 50. The viscosity contrast profile for case 3 as described in the caption to Fig. 49.

Fig. 51. The fluctuating temperature profile for case 3 as described in the caption to Fig. 49.

Fig. 52. The horizontal velocity profile for case 3 as described in the caption to Fig. 49.

Fig. 53. The vertical velocity profile for case 3 as described in the caption to Fig. 49.

Fig. 54. The geoid components as a function of age for case 3 as described in the caption to Fig. 49. The solid line is the total geoid anomaly, the dotted line is the upper-boundary-deformation contribution, the dashed line is the thermal contribution, and the dot-dashed line is the lower-boundary-deformation contribution.

Fig. 55. The topography as a function of age for case 3 as described in the caption to Fig. 49.

Fig. 56. The admittance as a function of age for case 3 as described in the caption to Fig. 49.

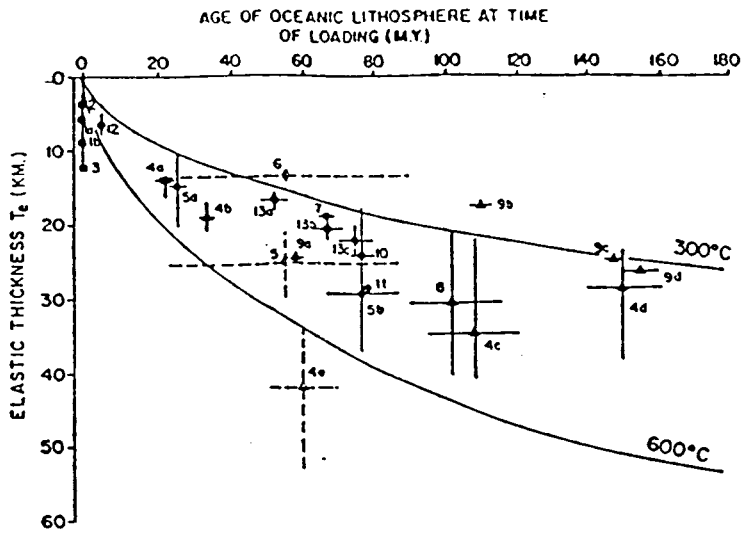

Figure 2

ORIGINAL PAGE IS
OF POOR QUALITY

SEASAT MEAN SEA SURFACE
MINUS GEM 10B (12,12) GEOID

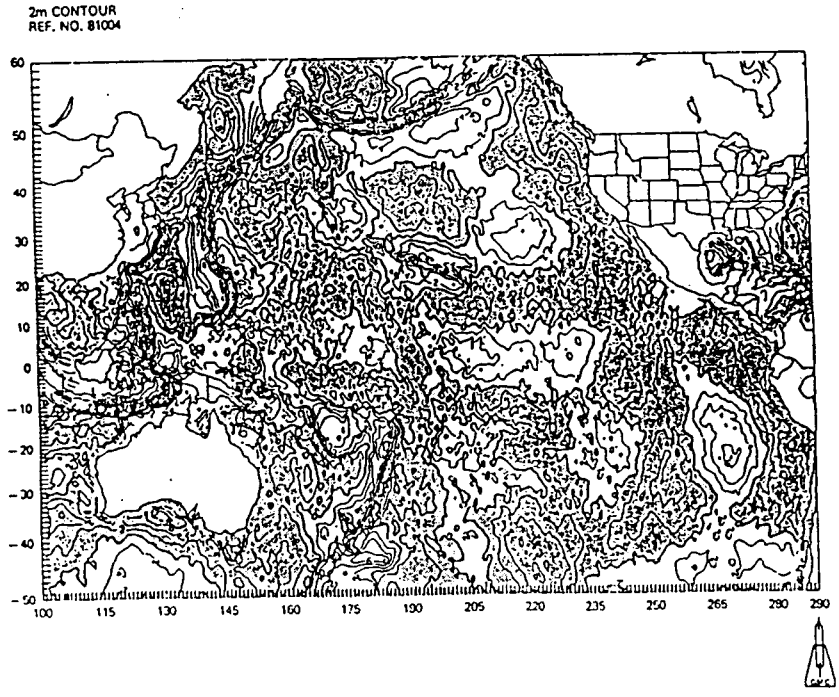

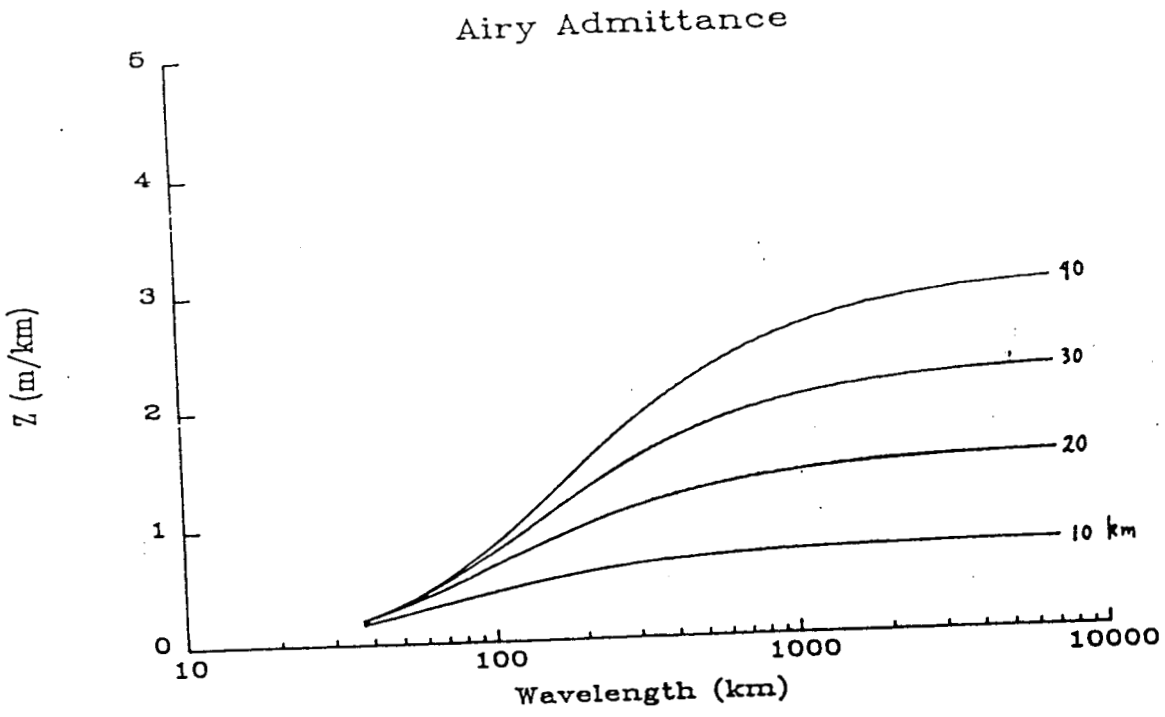
Airy Admittance
Z (m/km)
0
1
2
3
4
5
10
100
1000
10000
Wavelength (km)
40
30
20
10 km

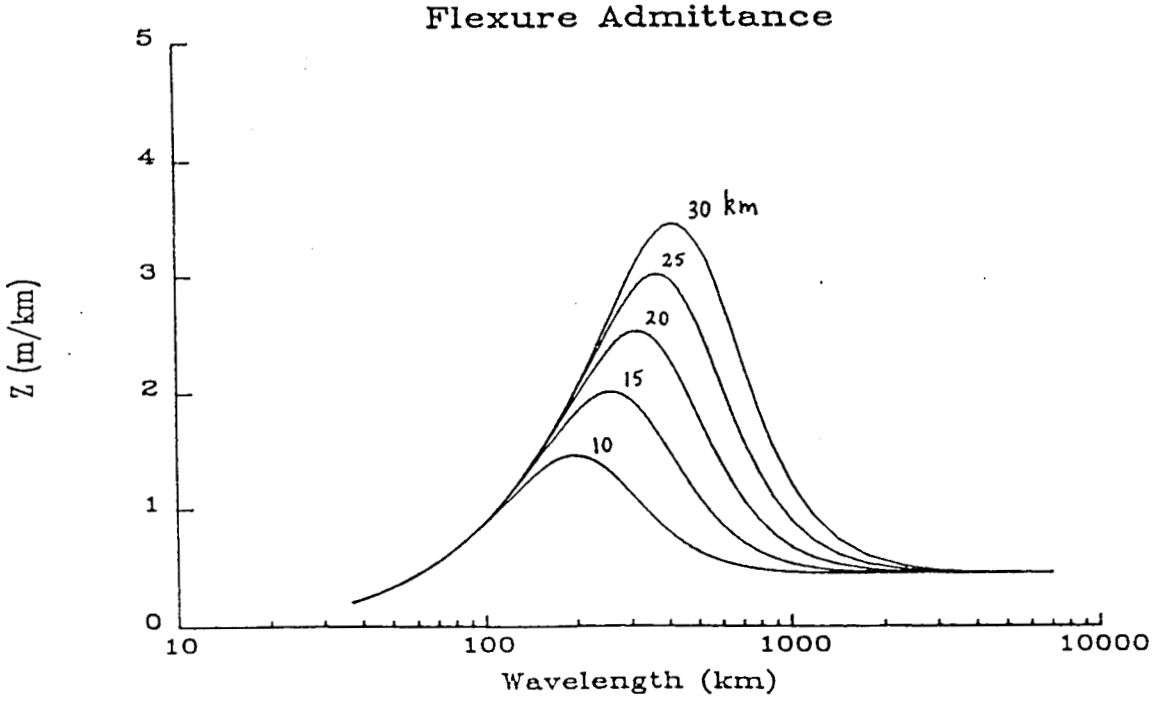
Flexure Admittance
Z (m/km)
0
1
2
3
4
5
10
100
1000
10000
Wavelength (km)
30 km
25
20
15
10

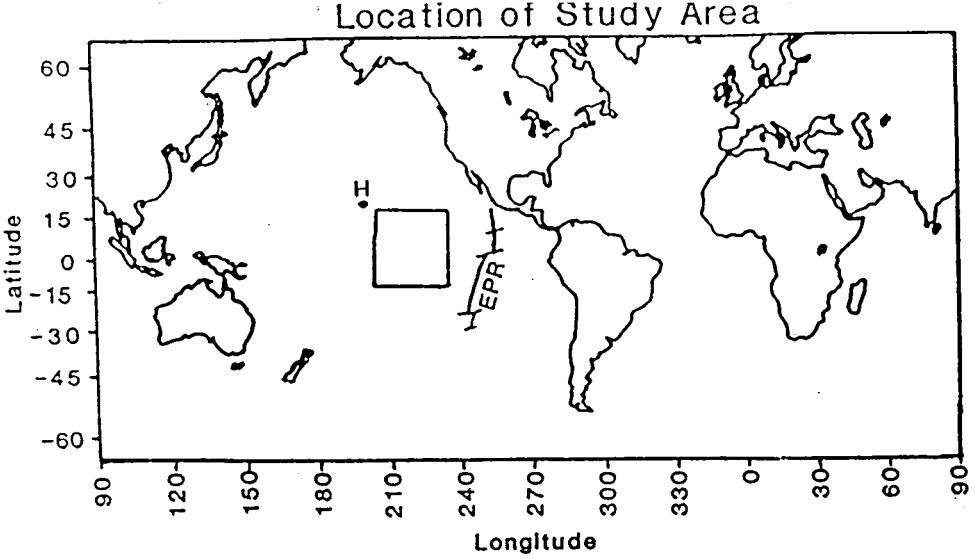
Location of Study Area
H
EPR
Latitude
Longitude
60
45
30
15
0
-15
-30
-45
-60
90
120
150
180
210
240
270
300
330
0
30
60
90

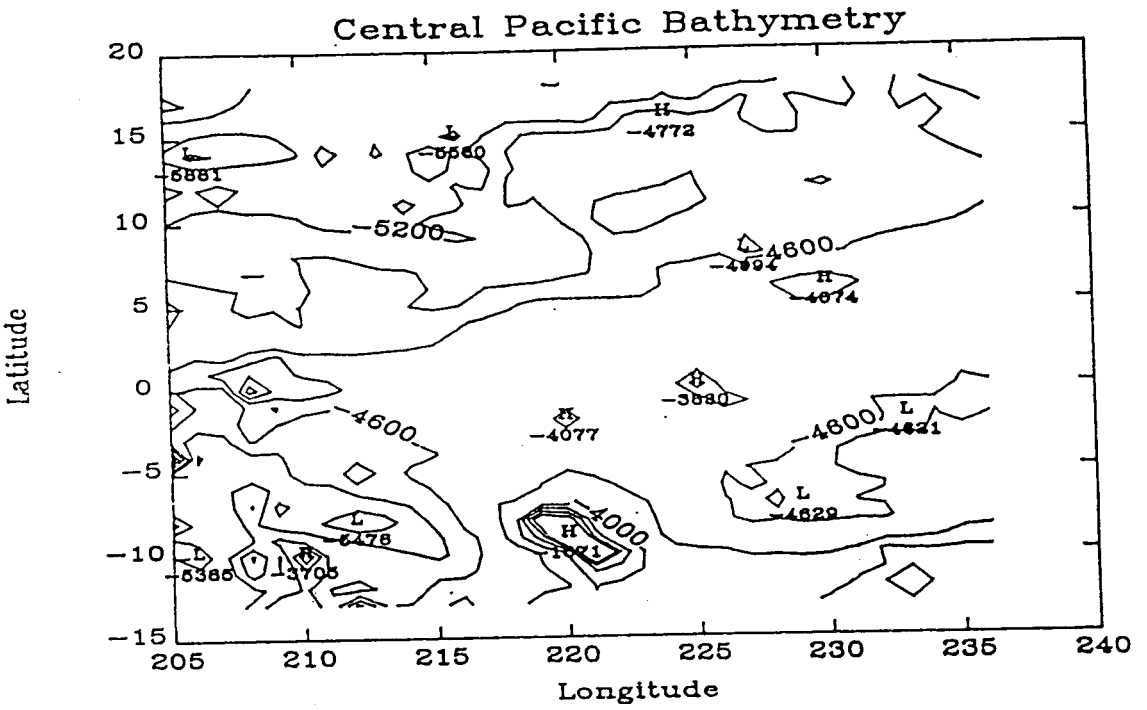
Central Pacific Bathymetry
Latitude
Longitude
-5200
-4600
-4000
-4772
-4077
-4074
-4629
-4621
-6478
-6386
-5705
-6881
20
15
10
5
0
-5
-10
-15
205
210
215
220
225
230
235
240

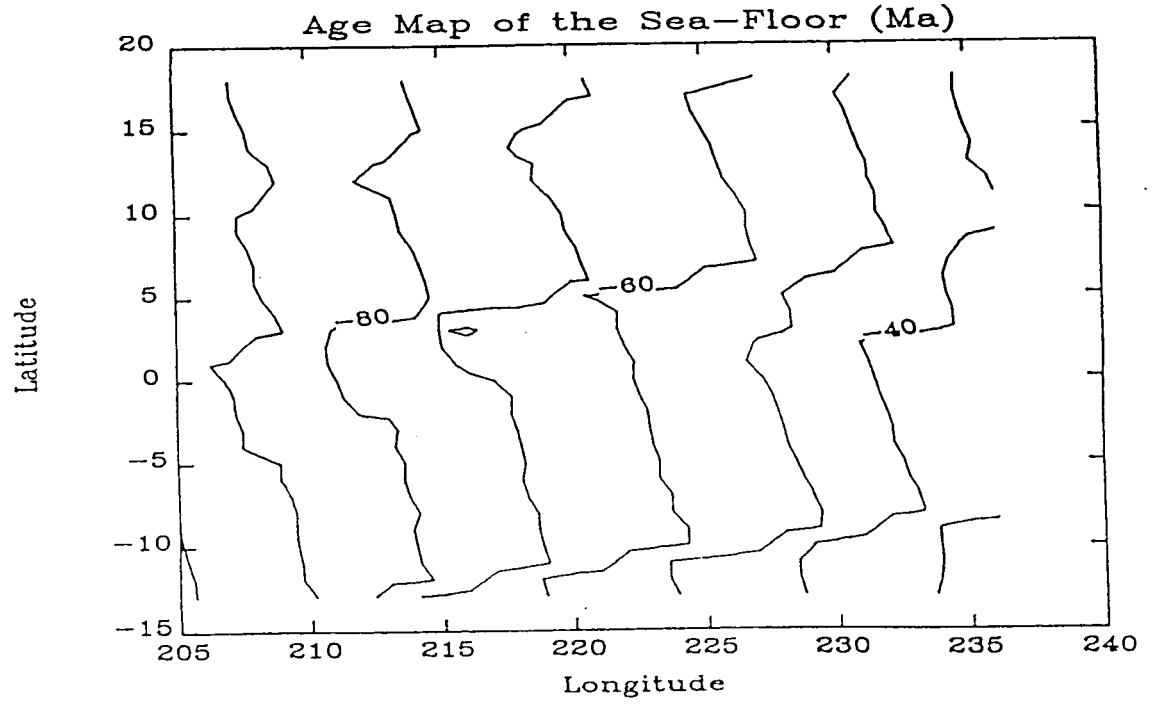
Age Map of the Sea—Floor (Ma)
Latitude
Longitude
-80
-60
-40
20
15
10
5
0
-5
-10
-15
205
210
215
220
225
230
235
240

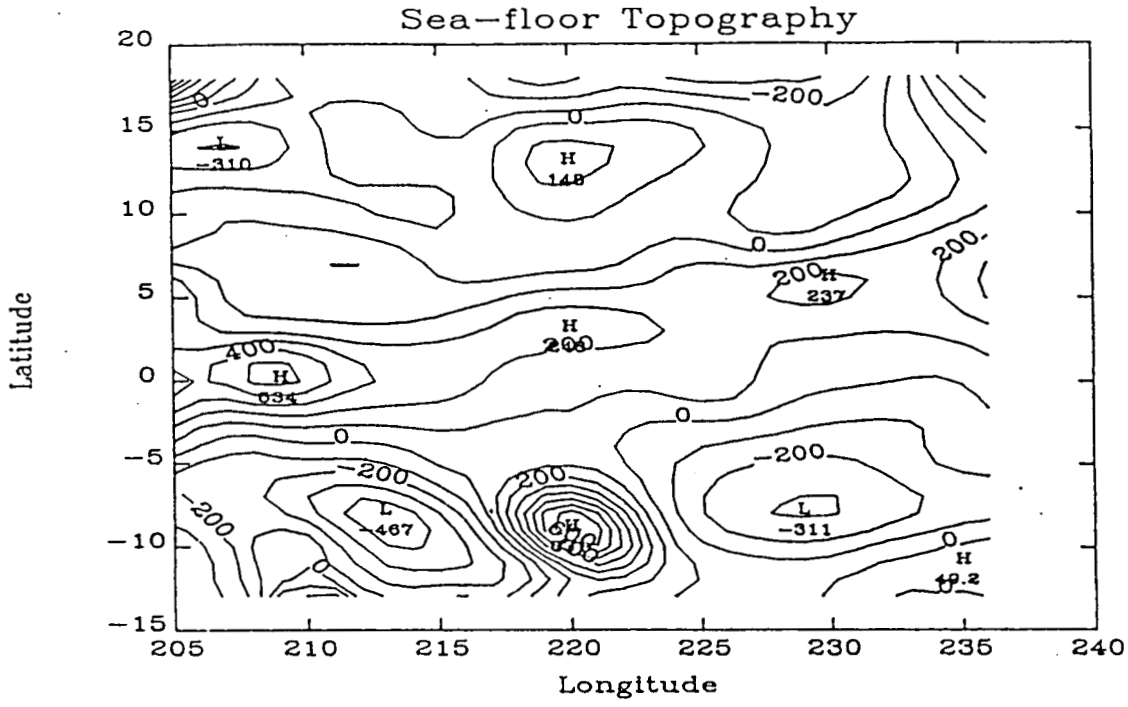
Sea–floor Topography
Latitude
Longitude
20
15
10
5
0
−5
−10
−15
205
210
215
220
225
230
235
240
−200
0
200
400
L
−310
H
148
H
237
H
208
H
034
L
−467
H
L
−311
H
49.2

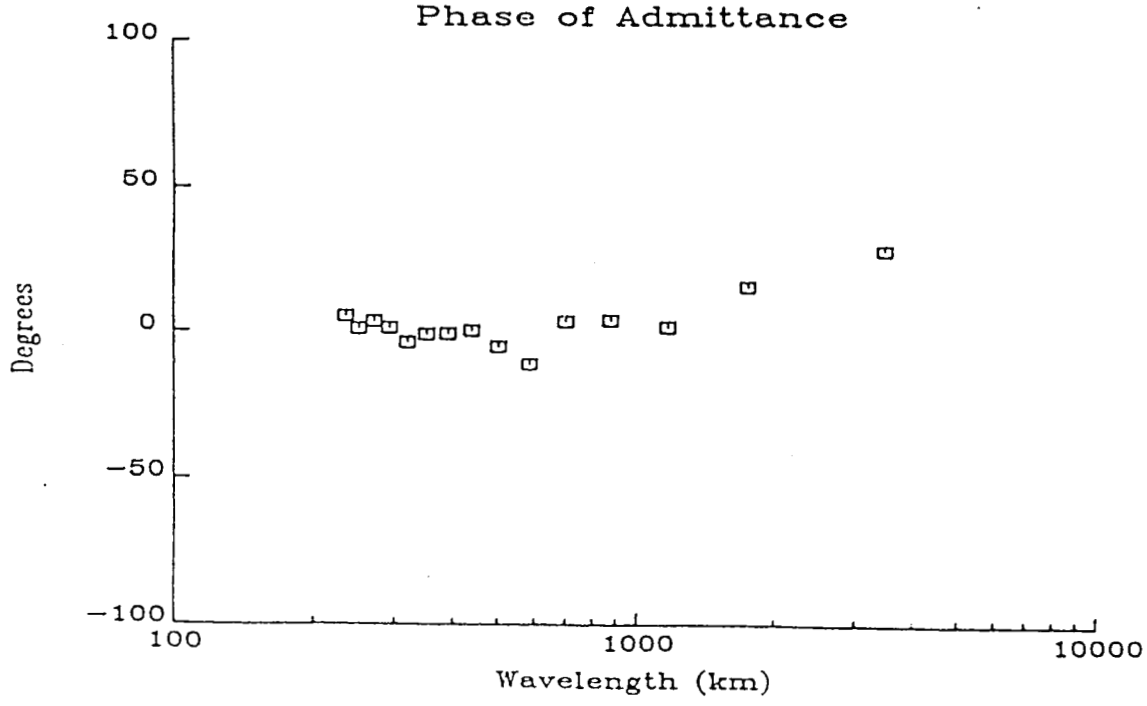
Phase of Admittance
Degrees
Wavelength (km)
100
50
0
−50
−100
100
1000
10000

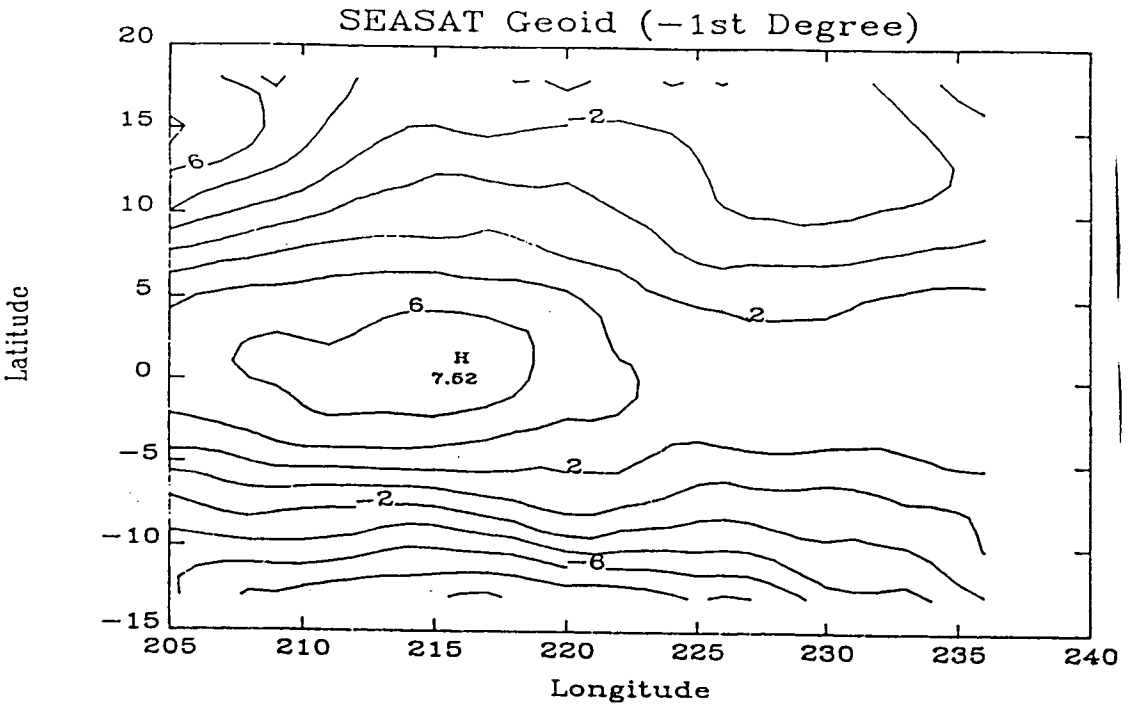
SEASAT Geoid (−1st Degree)
Latitude
Longitude
20
15
10
5
0
−5
−10
−15
205
210
215
220
225
230
235
240
H
7.62
6
2
−2
−6

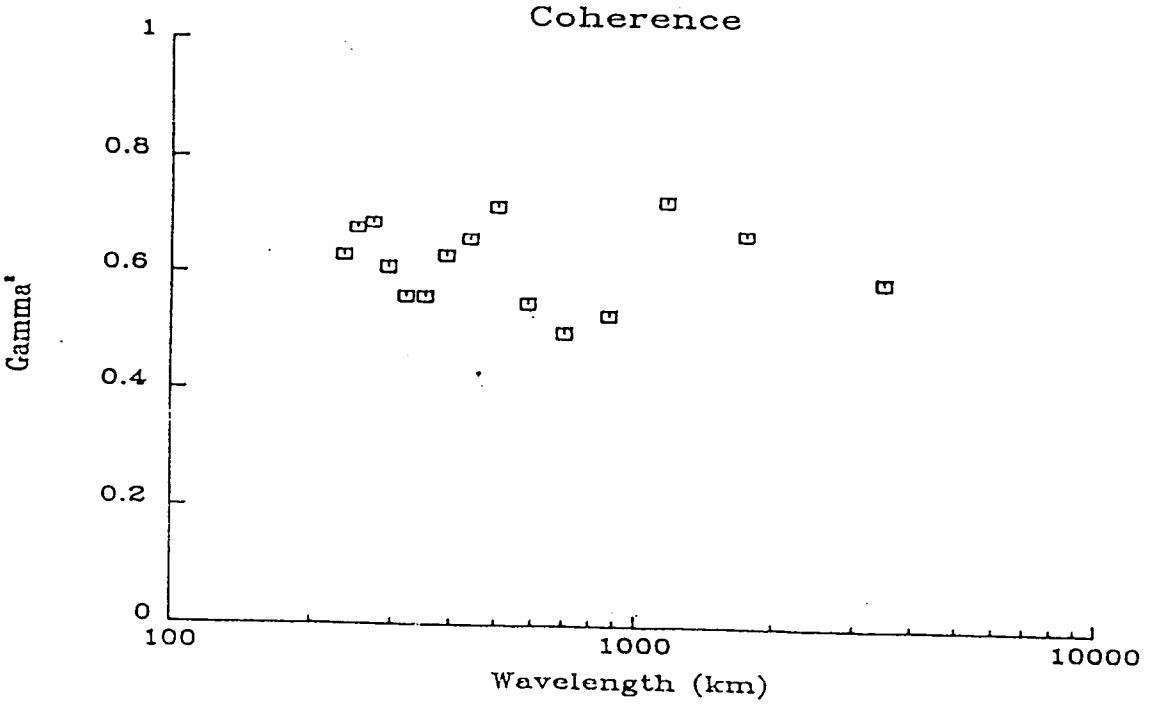
Coherence
Gamma²
Wavelength (km)
1
0.8
0.6
0.4
0.2
0
100
1000
10000

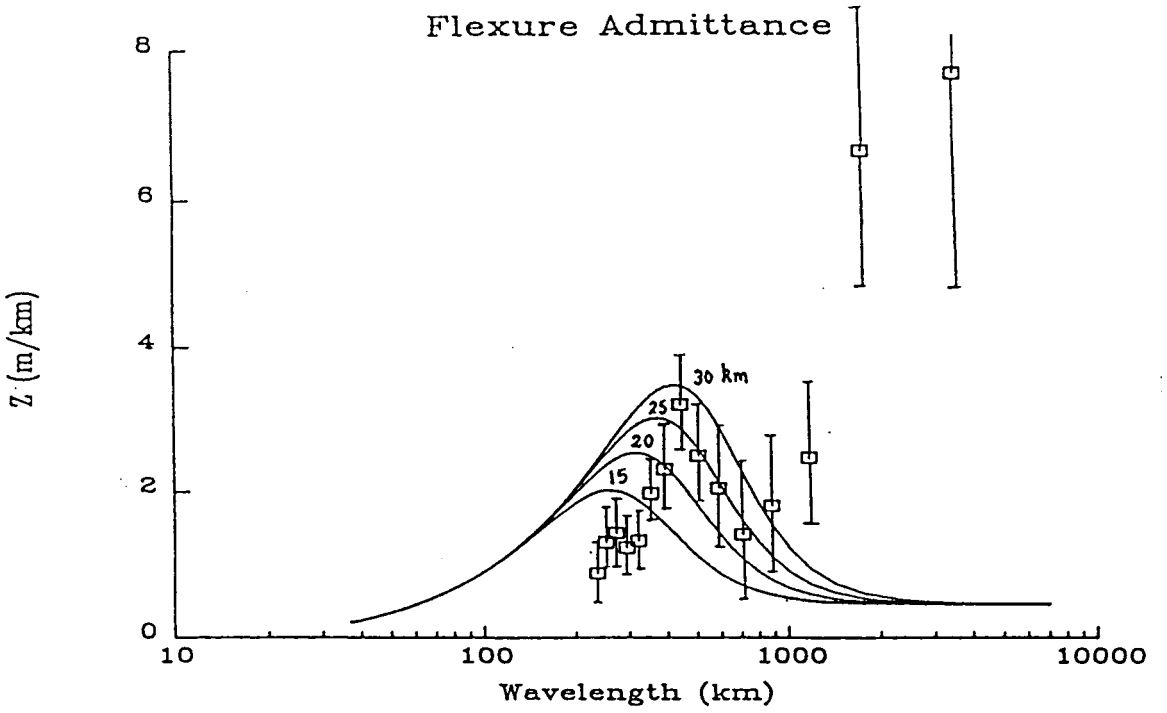
Flexure Admittance
Z (m/km)
8
6
4
2
0
30 km
25
20
15
10
100
1000
10000
Wavelength (km)

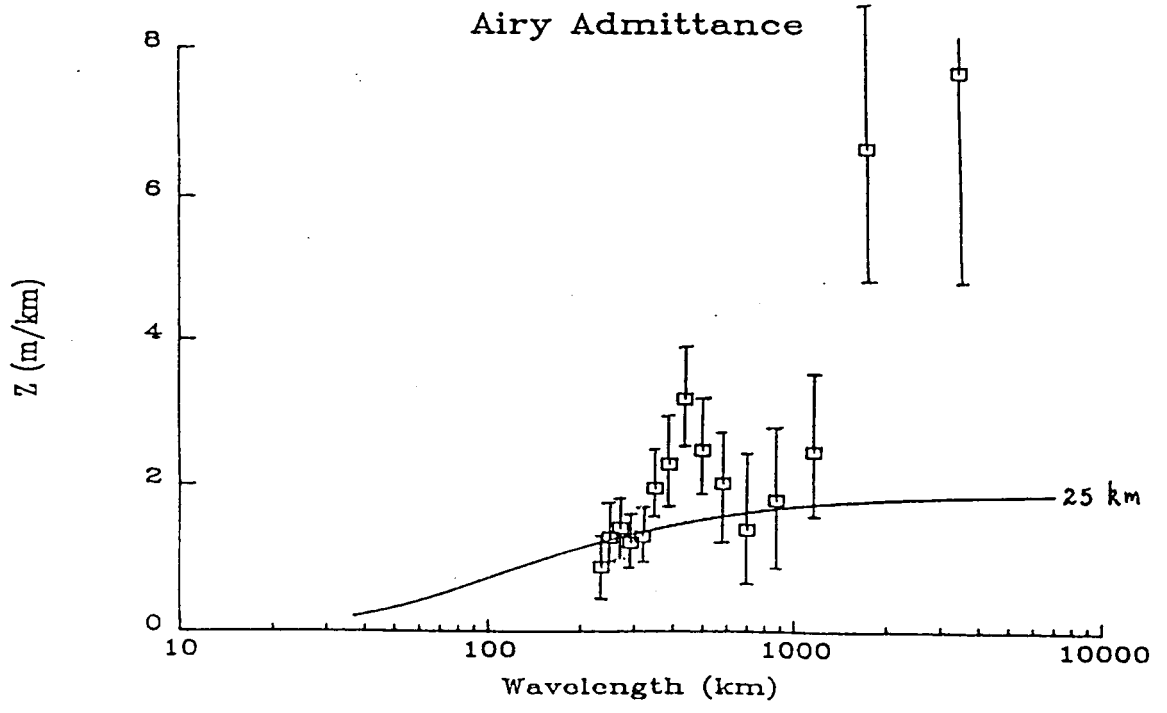
Airy Admittance
Z (m/km)
8
6
4
2
0
25 km
10
100
1000
10000
Wavelength (km)

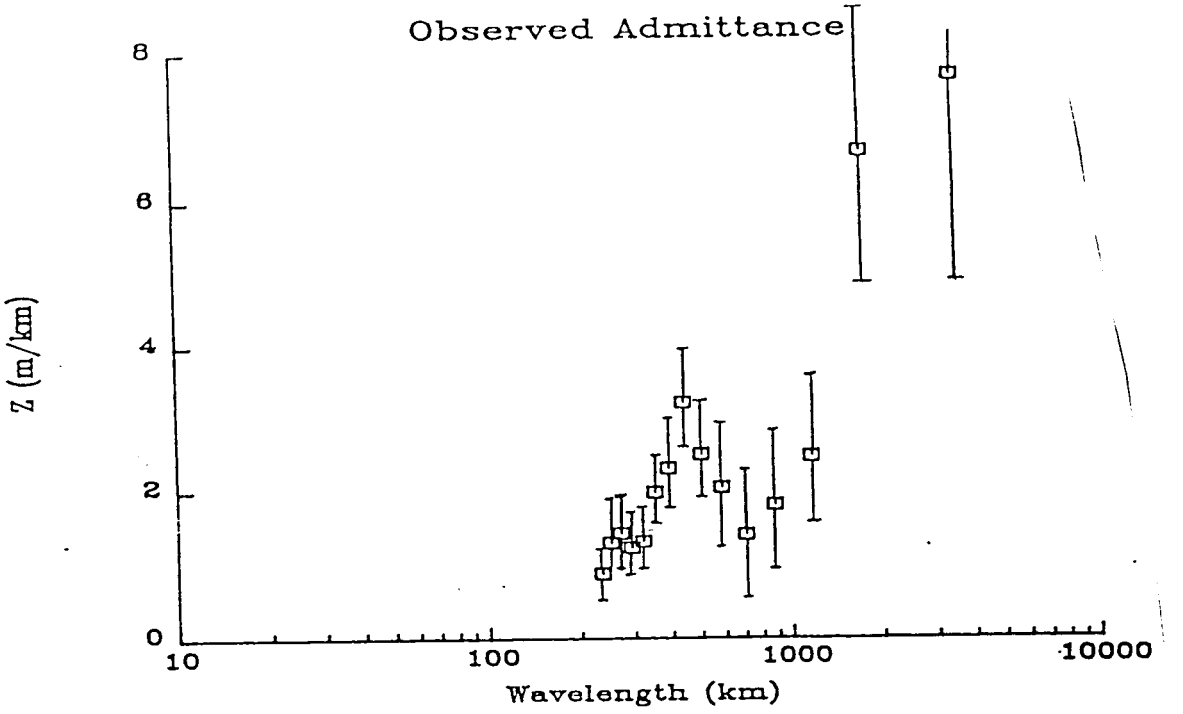
Observed Admittance
Z (m/km)
8
6
4
2
0
10
100
1000
10000
Wavelength (km)

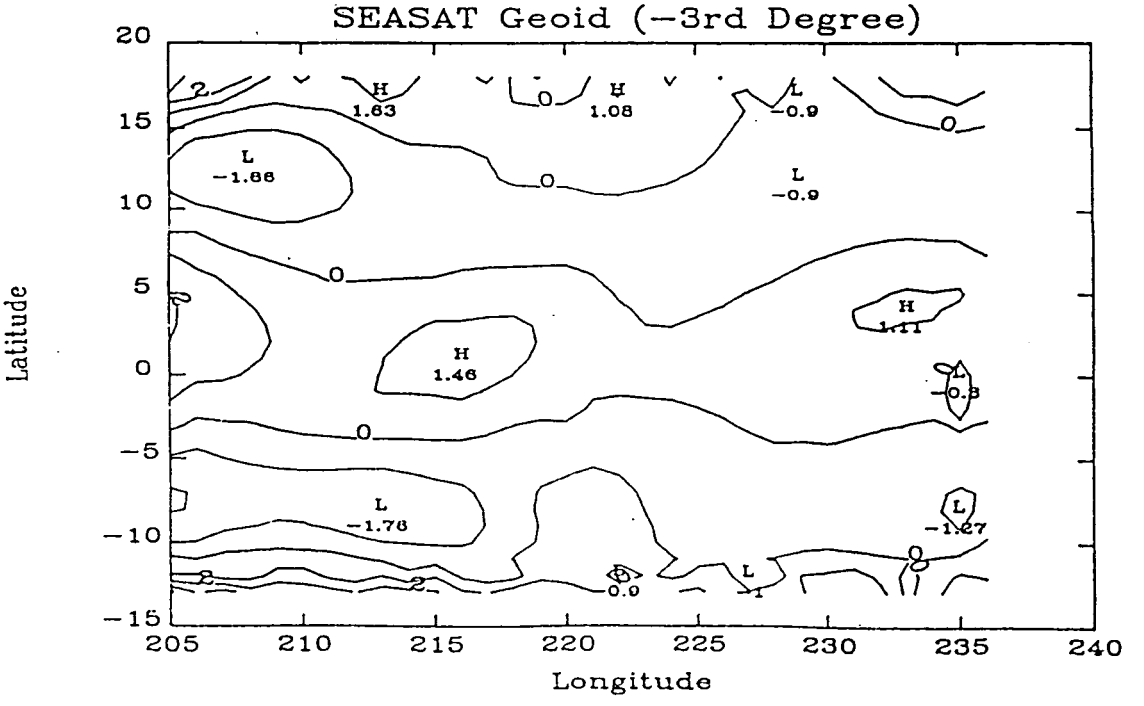
SEASAT Geoid (−3rd Degree)
Latitude
20
15
10
5
0
−5
−10
−15
205
210
215
220
225
230
235
240
Longitude
H
1.63
H
1.08
L
−0.9
L
−1.66
L
−0.9
H
1.11
H
1.46
L
−0.3
L
−1.76
L
−1.27
0.9
L
−1

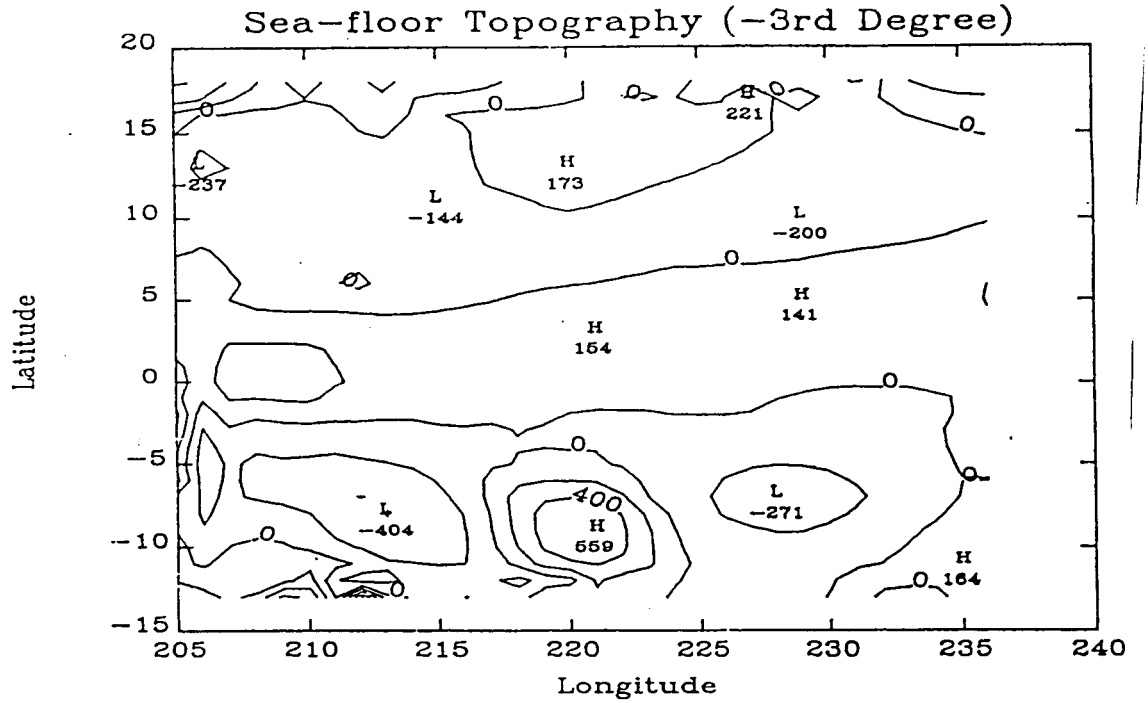
Sea-floor Topography (-3rd Degree)
Latitude
Longitude
20
15
10
5
0
-5
-10
-15
205
210
215
220
225
230
235
240
H
221
H
173
L
-144
L
-200
-237
H
141
H
154
L
-404
400
H
659
L
-271
H
164

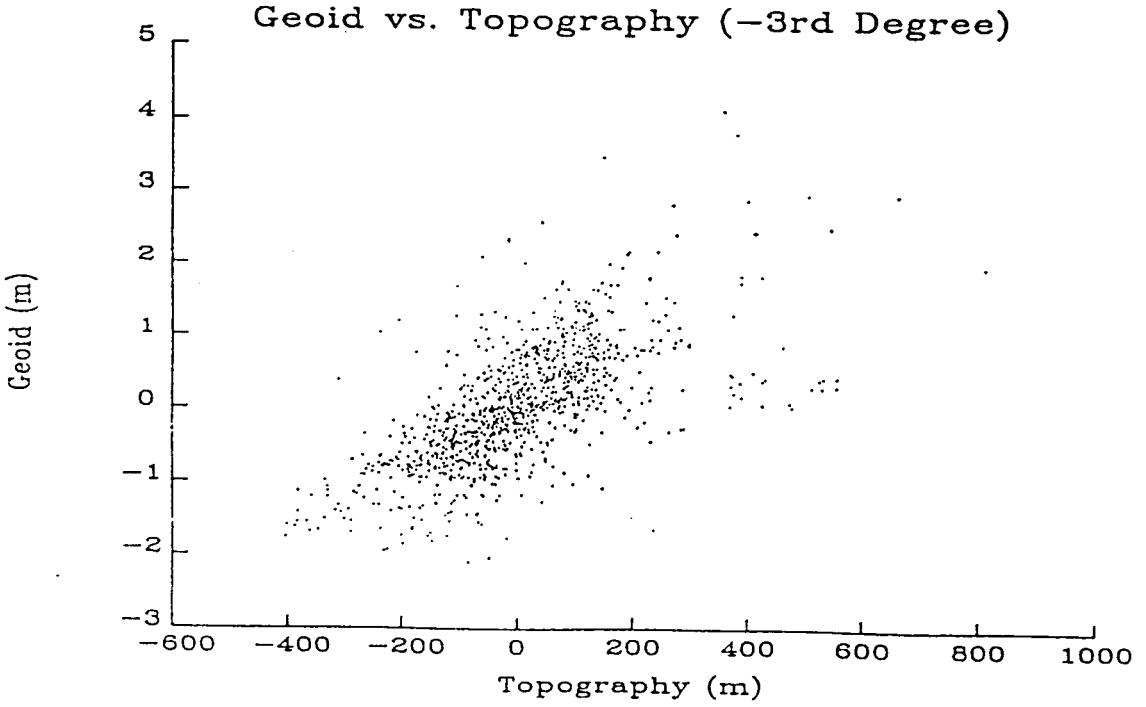
Geoid vs. Topography (-3rd Degree)
Geoid (m)
Topography (m)
5
4
3
2
1
0
-1
-2
-3
-600
-400
-200
0
200
400
600
800
1000

Upper-mantle Convection Model

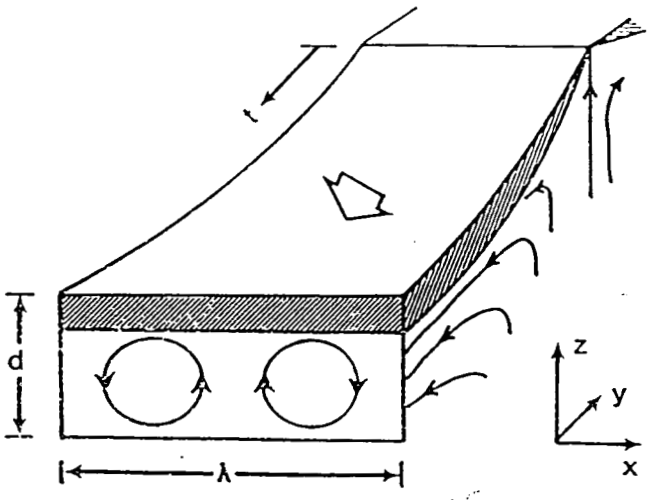

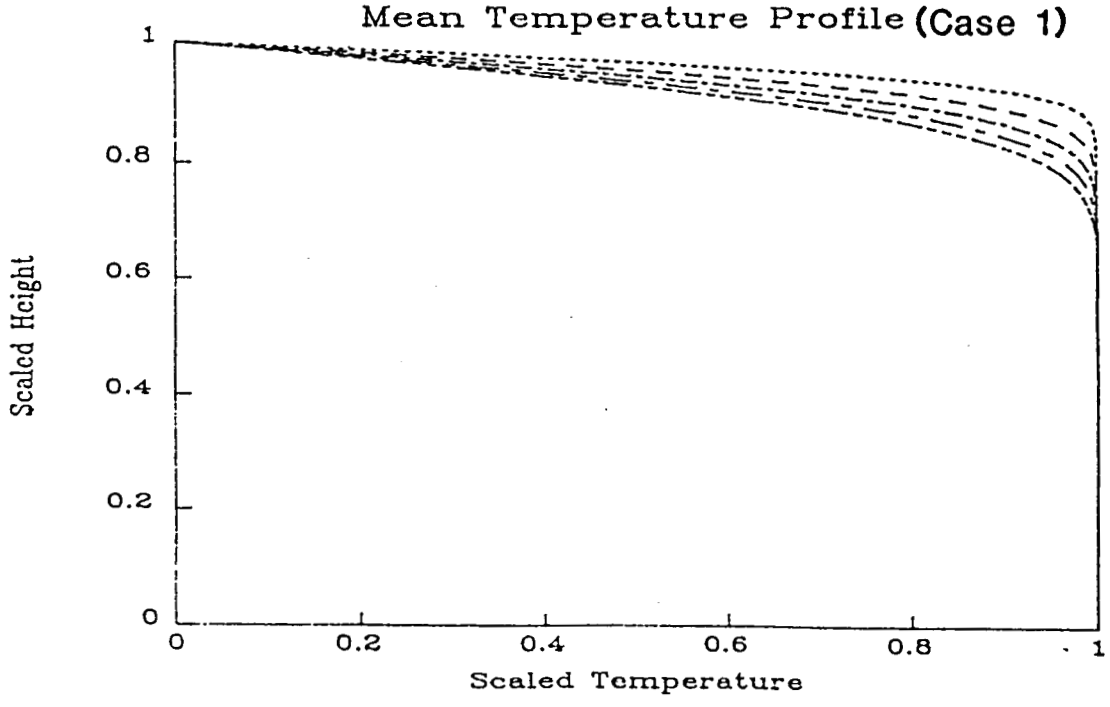

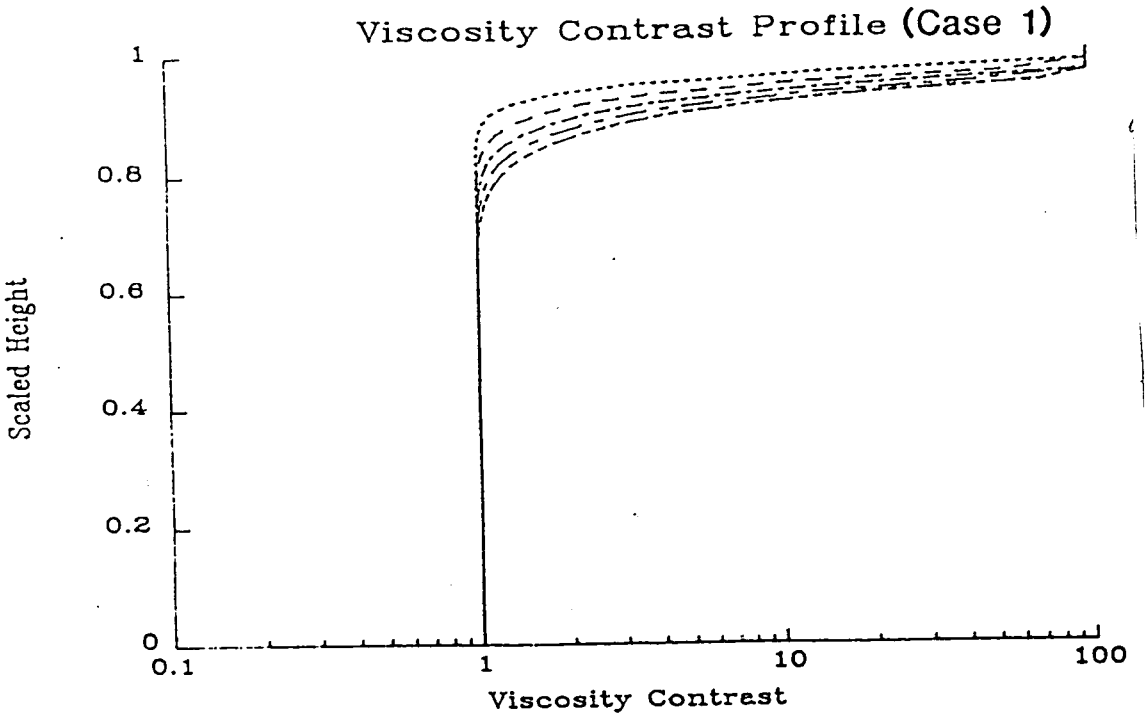
Viscosity Contrast Profile (Case 1)
Scaled Height
1
0.8
0.6
0.4
0.2
0
0.1
1
10
100
Viscosity Contrast

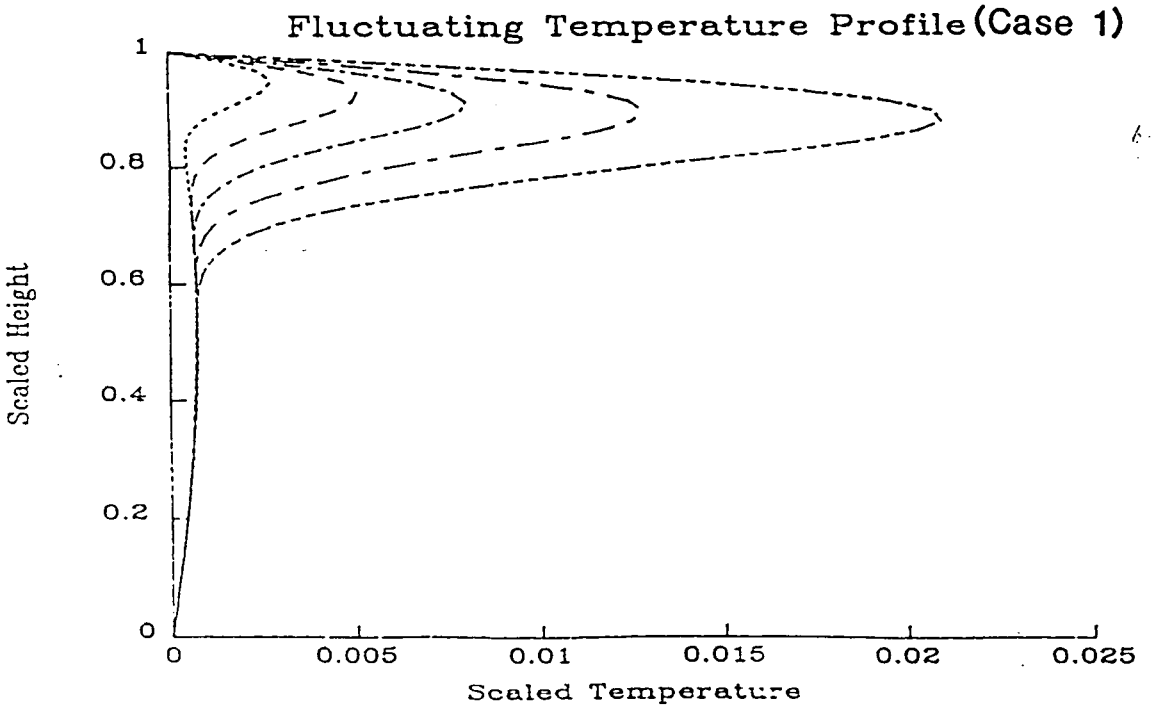
Fluctuating Temperature Profile (Case 1)
Scaled Height
1
0.8
0.6
0.4
0.2
0
0
0.005
0.01
0.015
0.02
0.025
Scaled Temperature

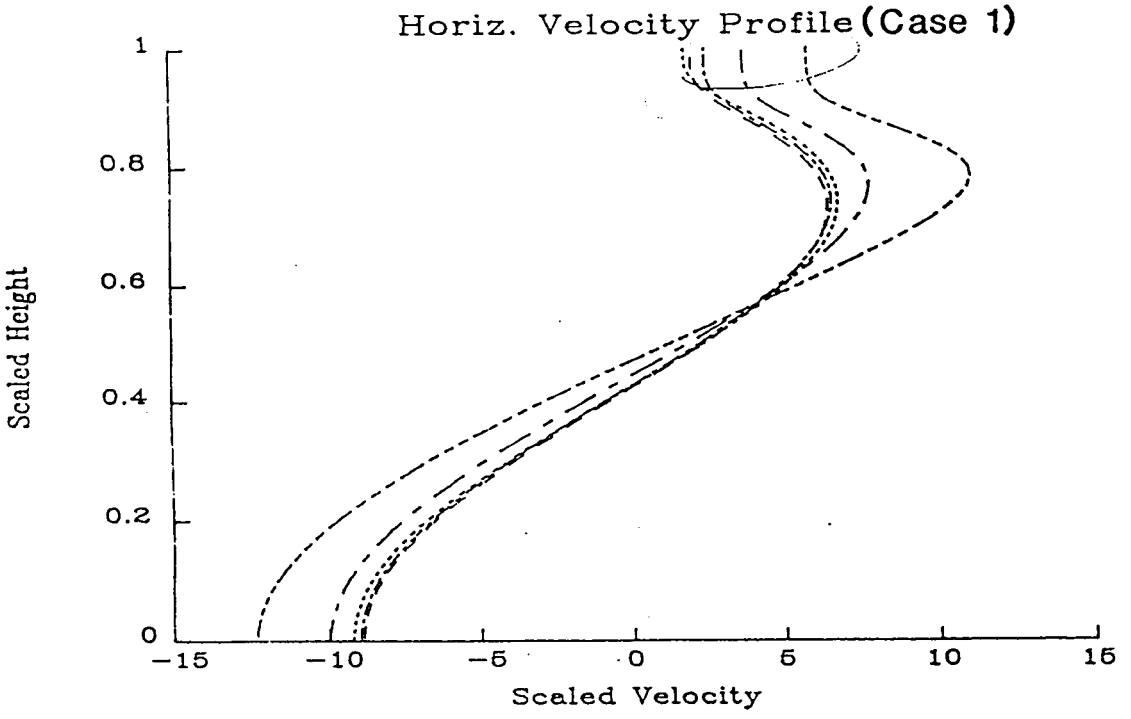
Horiz. Velocity Profile (Case 1)
Scaled Height
1
0.8
0.6
0.4
0.2
0
−15
−10
−5
0
5
10
15
Scaled Velocity

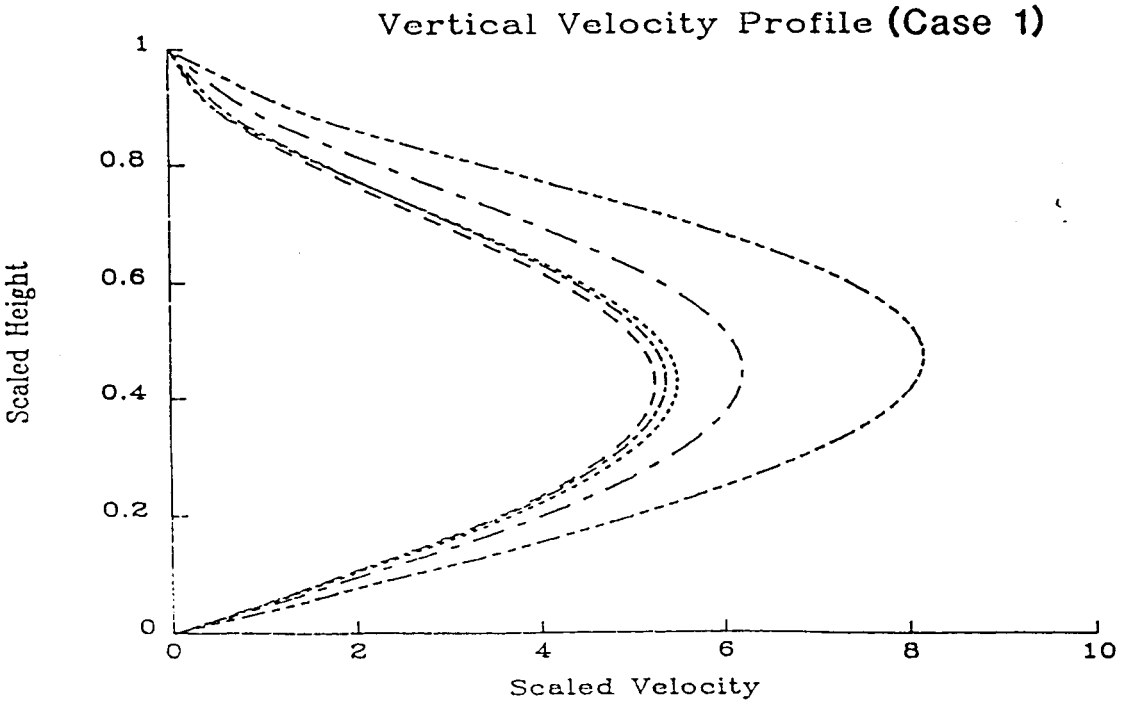
Vertical Velocity Profile (Case 1)
Scaled Height
1
0.8
0.6
0.4
0.2
0
0
2
4
6
8
10
Scaled Velocity

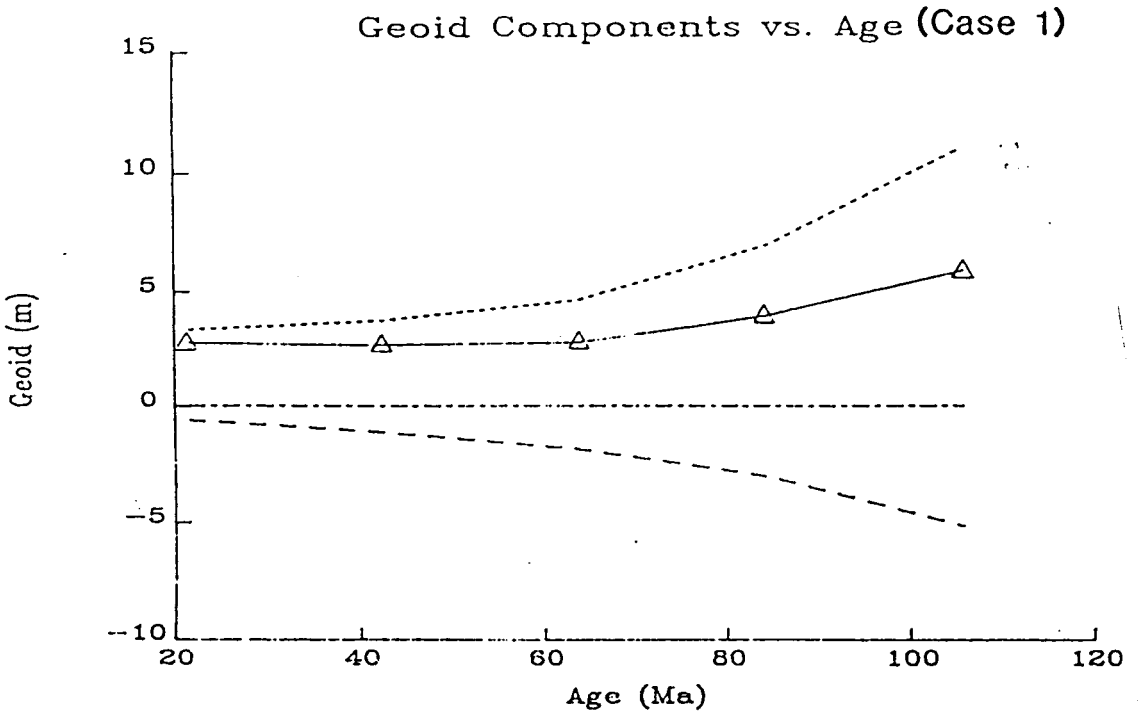
Geoid Components vs. Age (Case 1)
Geoid (m)
15
10
5
0
−5
−10
20
40
60
80
100
120
Age (Ma)

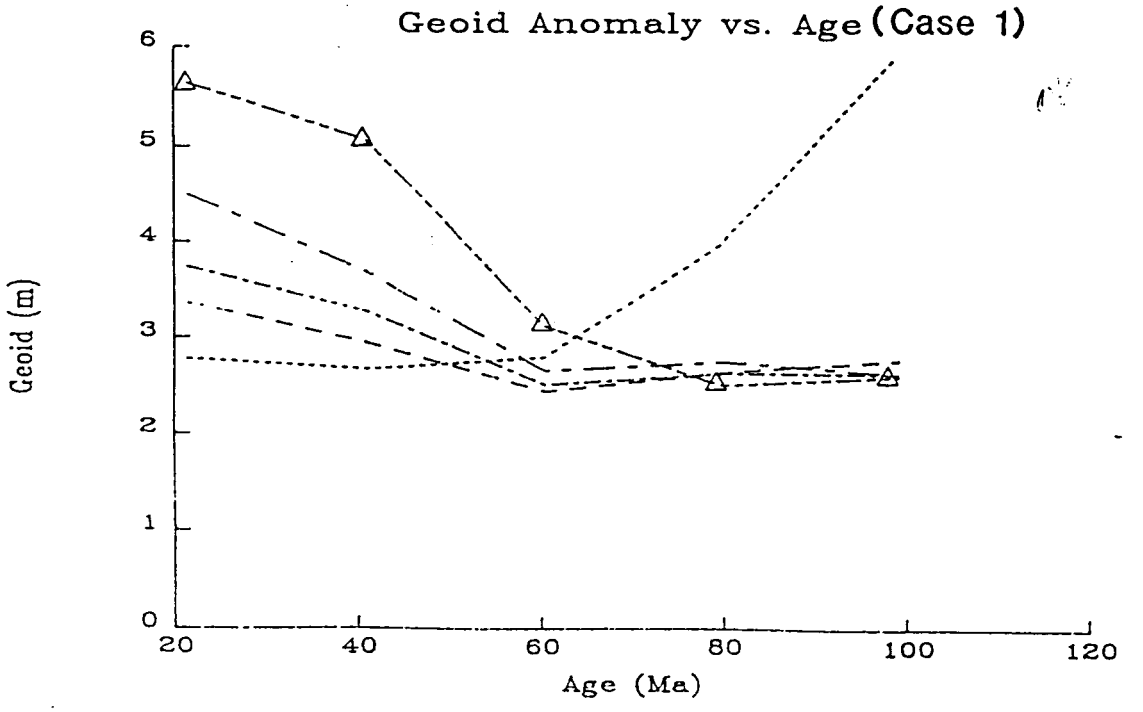
Geoid Anomaly vs. Age (Case 1)
Geoid (m)
6
5
4
3
2
1
0
20
40
60
80
100
120
Age (Ma)

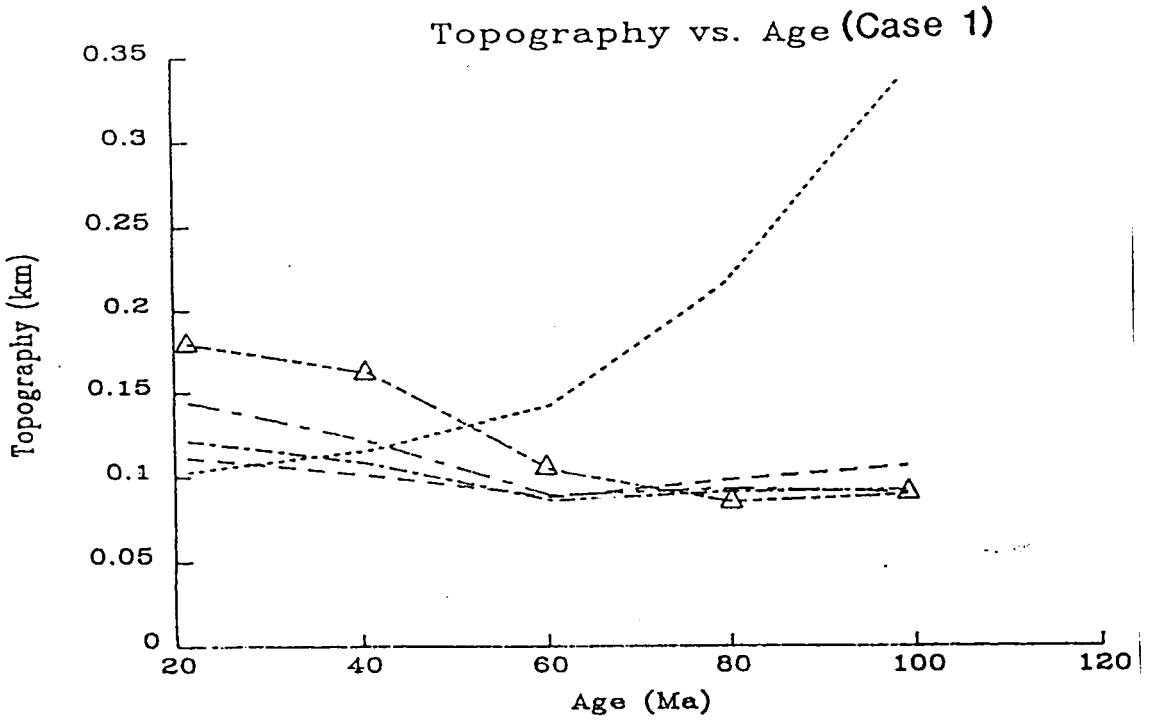
Topography vs. Age (Case 1)
Topography (km)
0.35
0.3
0.25
0.2
0.15
0.1
0.05
0
20
40
60
80
100
120
Age (Ma)

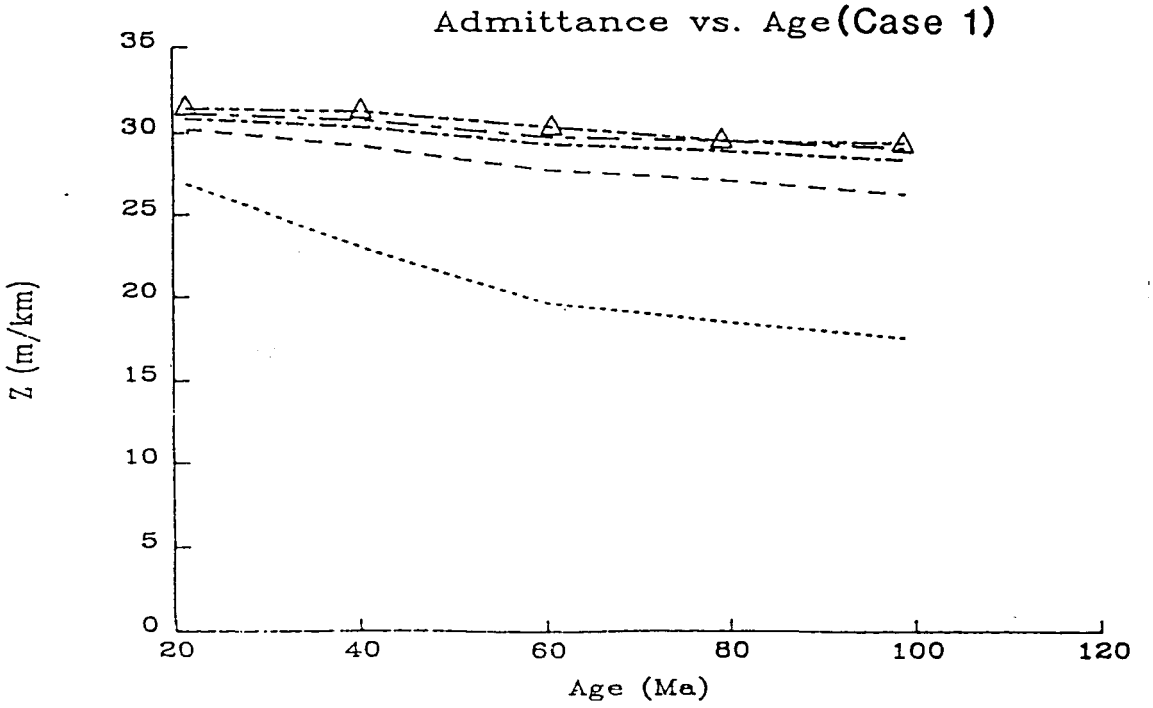
Admittance vs. Age (Case 1)
Z (m/km)
35
30
25
20
15
10
5
0
20
40
60
80
100
120
Age (Ma)

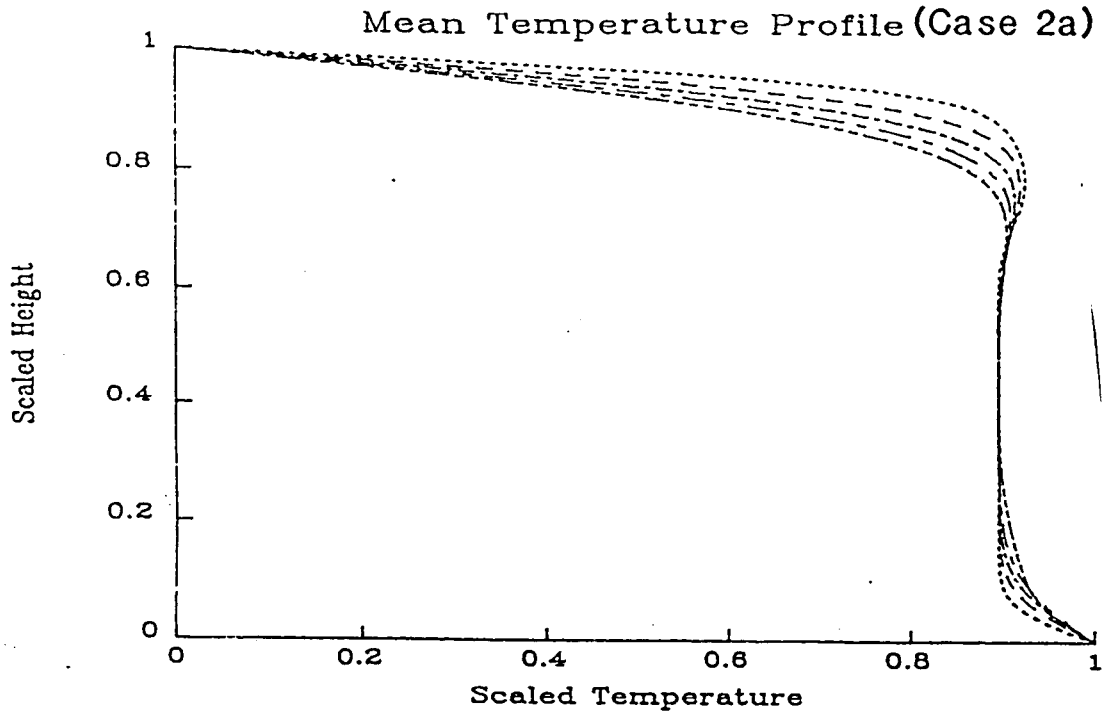
Mean Temperature Profile (Case 2a)
Scaled Height
1
0.8
0.6
0.4
0.2
0
0
0.2
0.4
0.6
0.8
1
Scaled Temperature

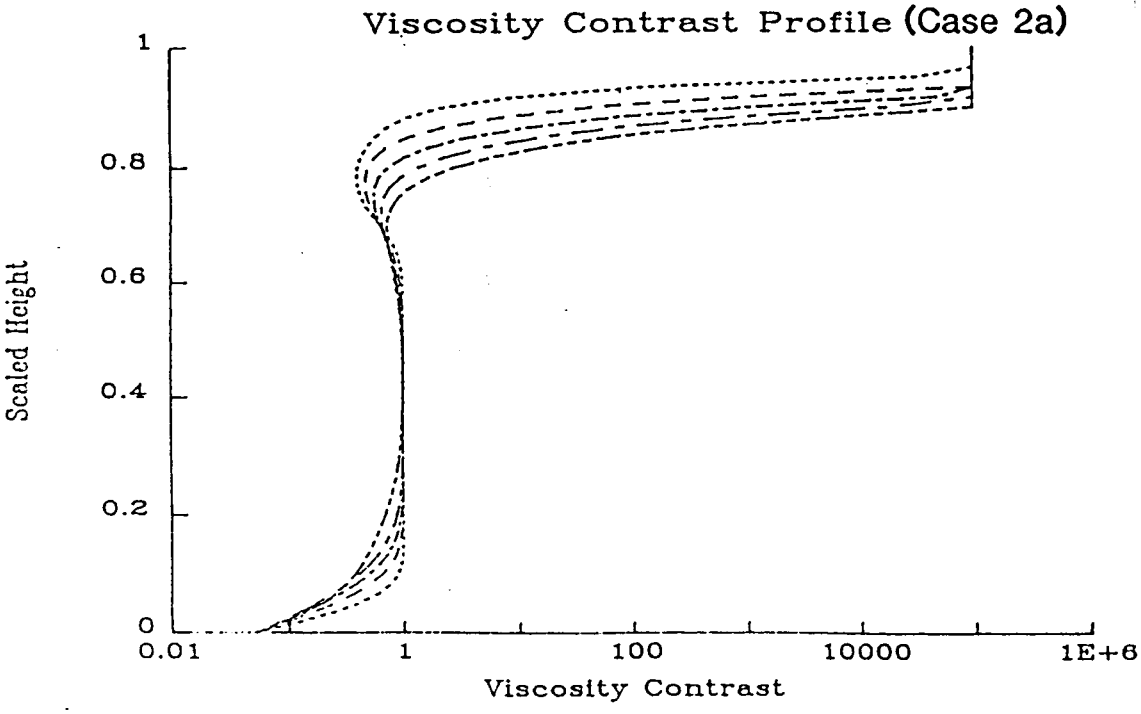
Viscosity Contrast Profile (Case 2a)
Scaled Height
1
0.8
0.6
0.4
0.2
0
0.01
1
100
10000
1E+6
Viscosity Contrast

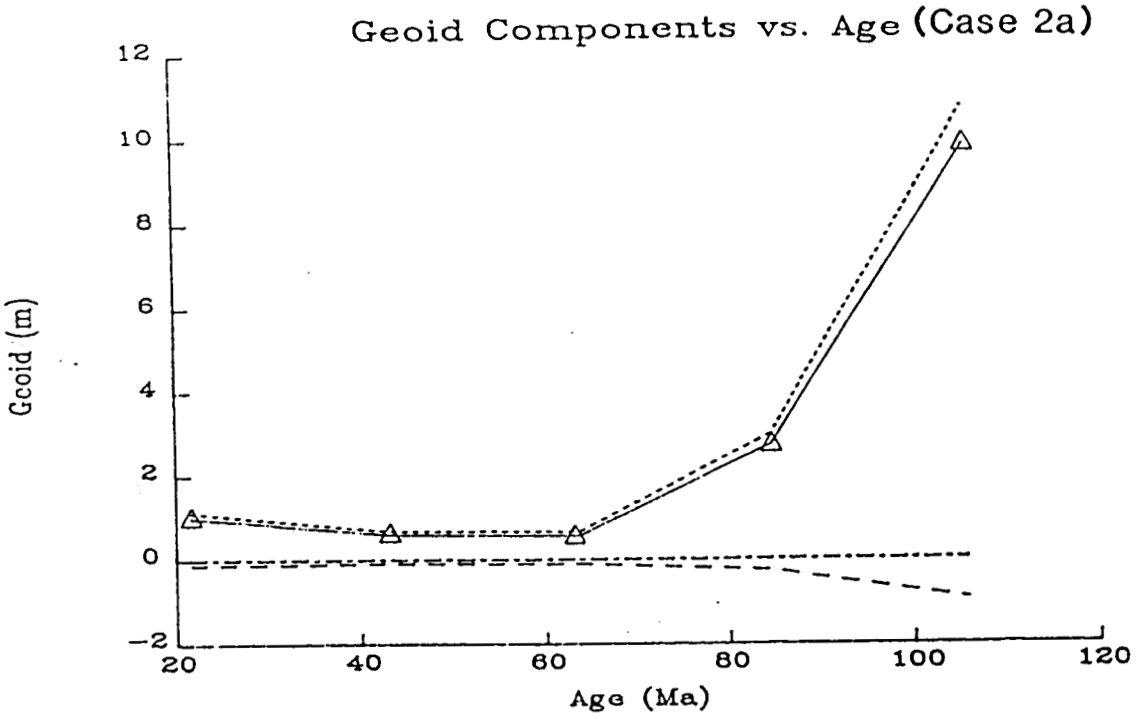
Geoid Components vs. Age (Case 2a)
Geoid (m)
12
10
8
6
4
2
0
−2
20
40
60
80
100
120
Age (Ma)

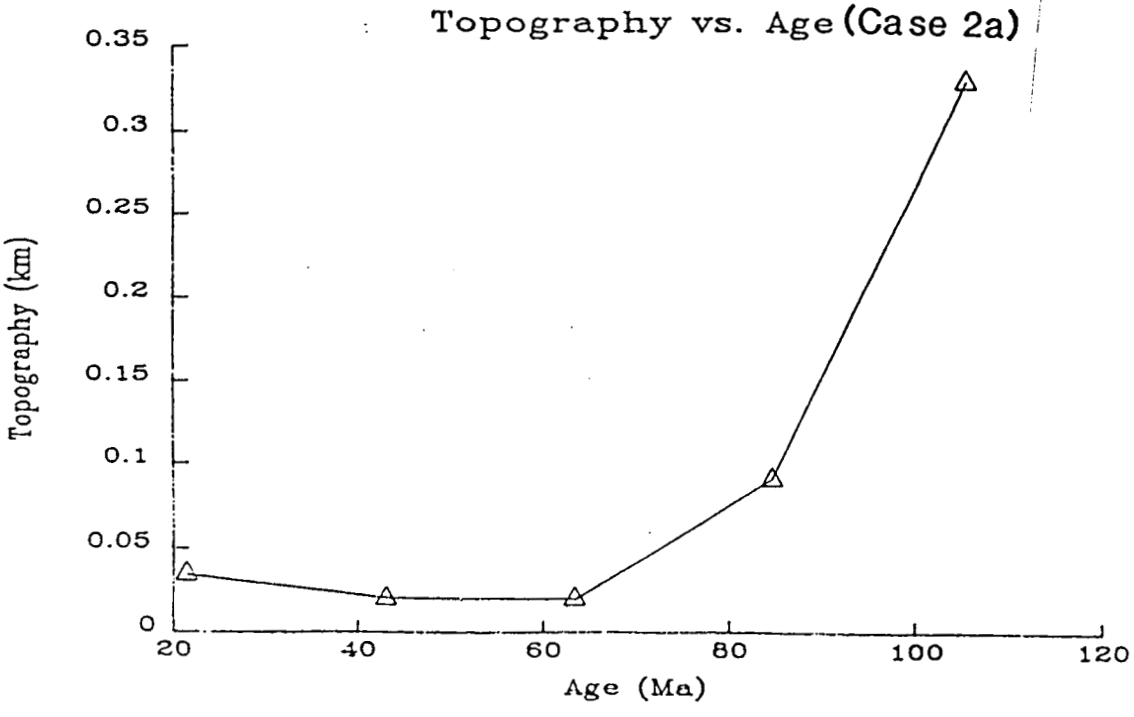
Topography vs. Age (Case 2a)
Topography (km)
0.35
0.3
0.25
0.2
0.15
0.1
0.05
0
20
40
60
80
100
120
Age (Ma)

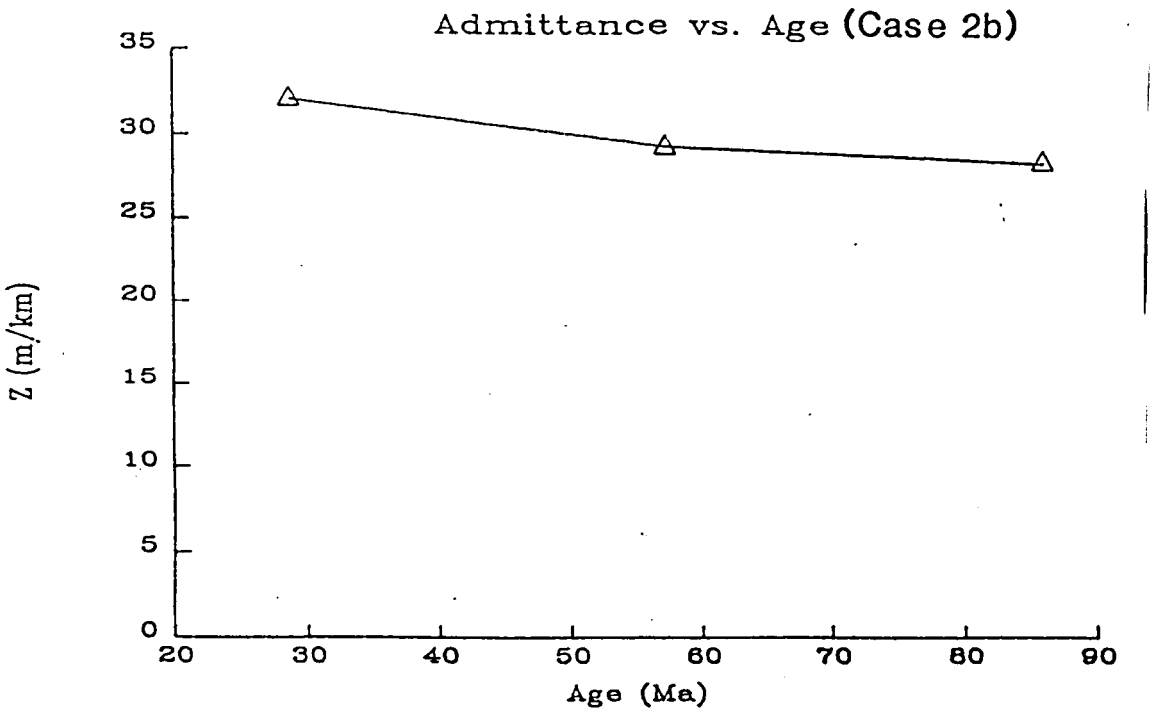
Admittance vs. Age (Case 2b)
Z (m/km)
35
30
25
20
15
10
5
0
20
30
40
50
60
70
80
90
Age (Ma)

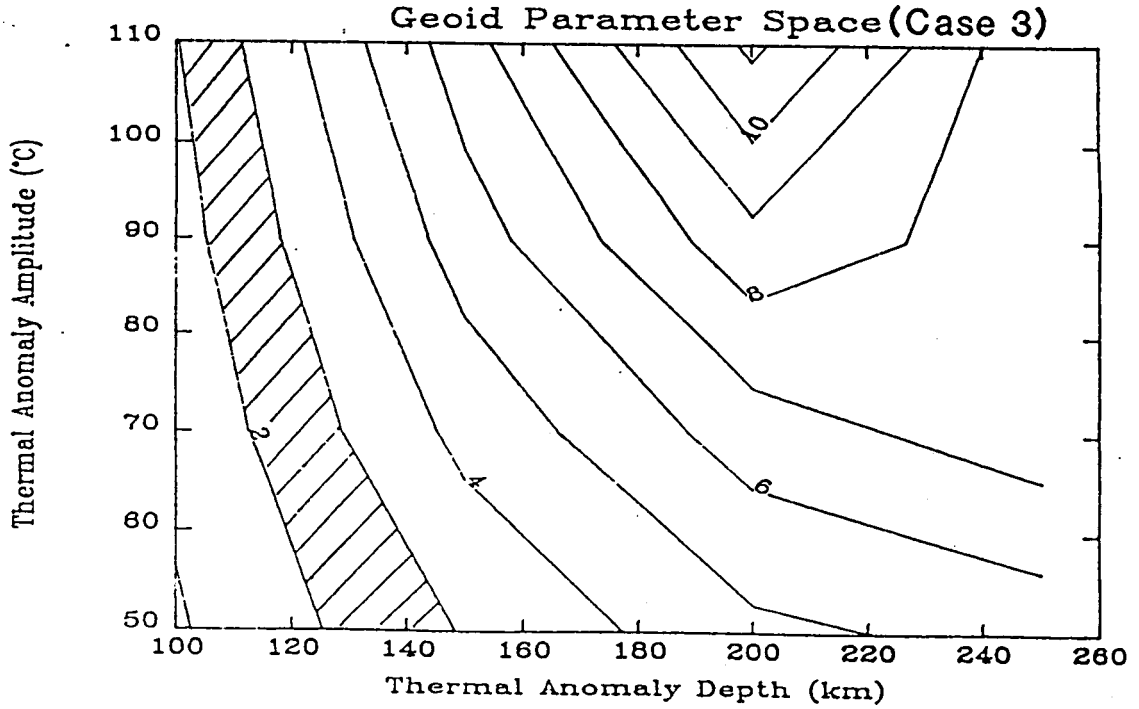
Geoid Parameter Space (Case 3)
Thermal Anomaly Amplitude (°C)
110
100
90
80
70
60
50
100
120
140
160
180
200
220
240
260
Thermal Anomaly Depth (km)
2
4
6
8
10

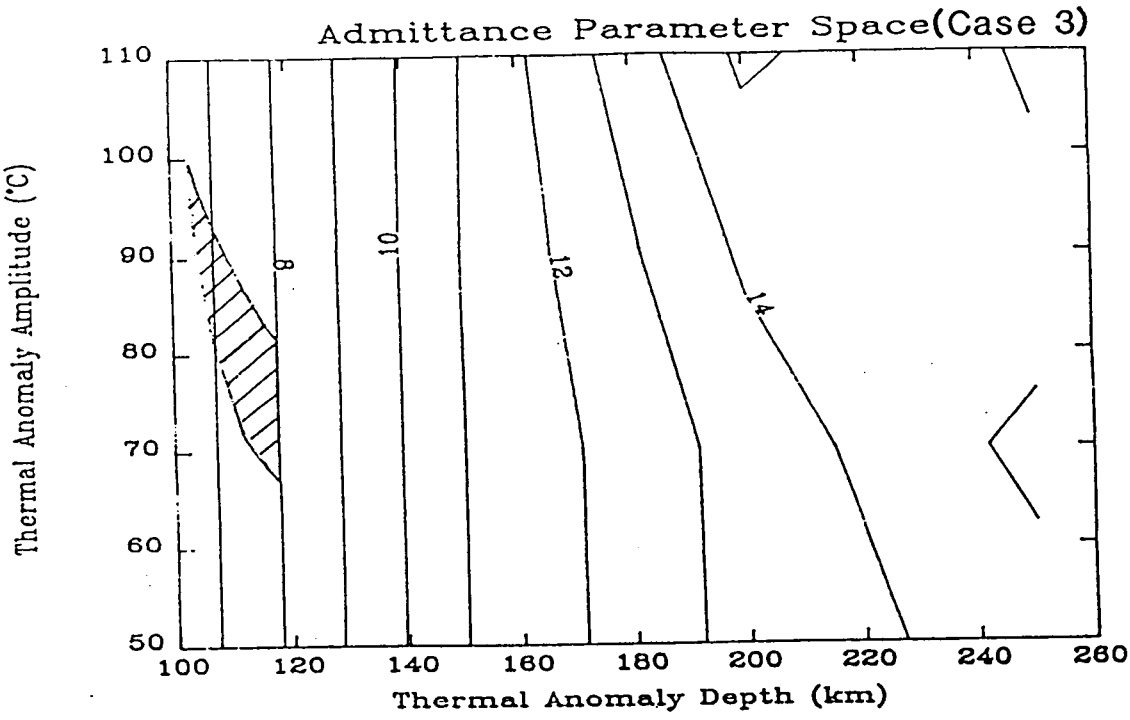
Admittance Parameter Space(Case 3)
Thermal Anomaly Amplitude (°C)
110
100
90
80
70
60
50
8
10
12
14
100
120
140
160
180
200
220
240
260
Thermal Anomaly Depth (km)

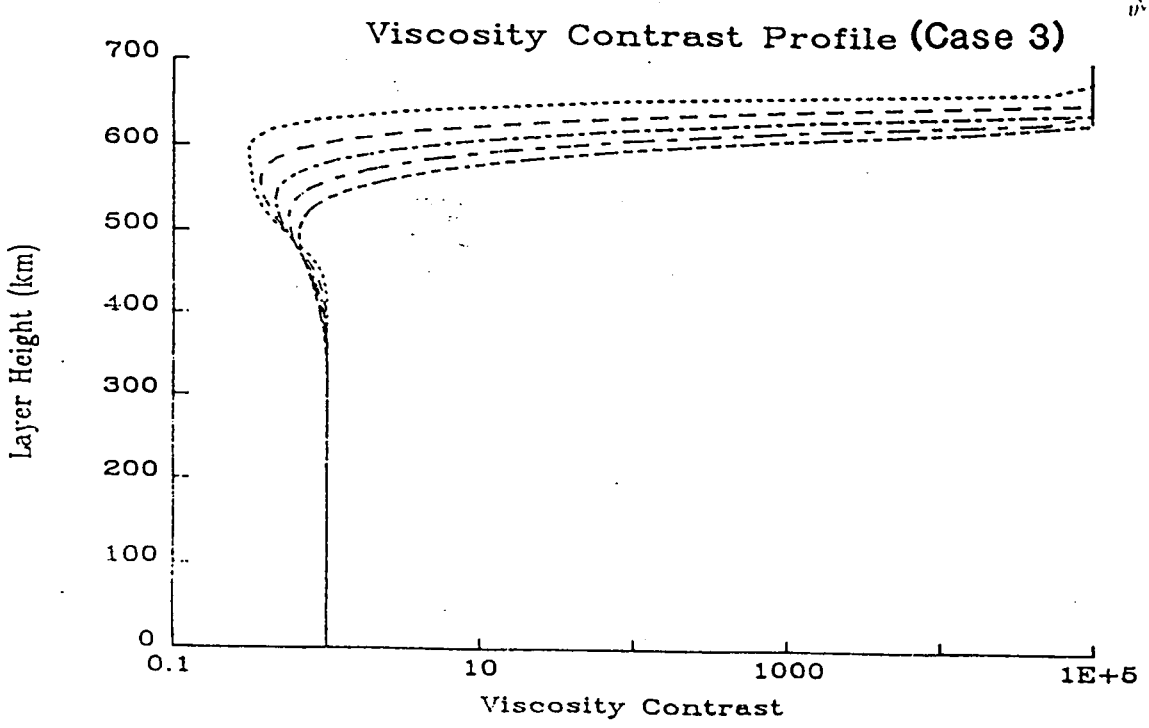
Viscosity Contrast Profile (Case 3)
Layer Height (km)
700
600
500
400
300
200
100
0
0.1
10
1000
1E+5
Viscosity Contrast

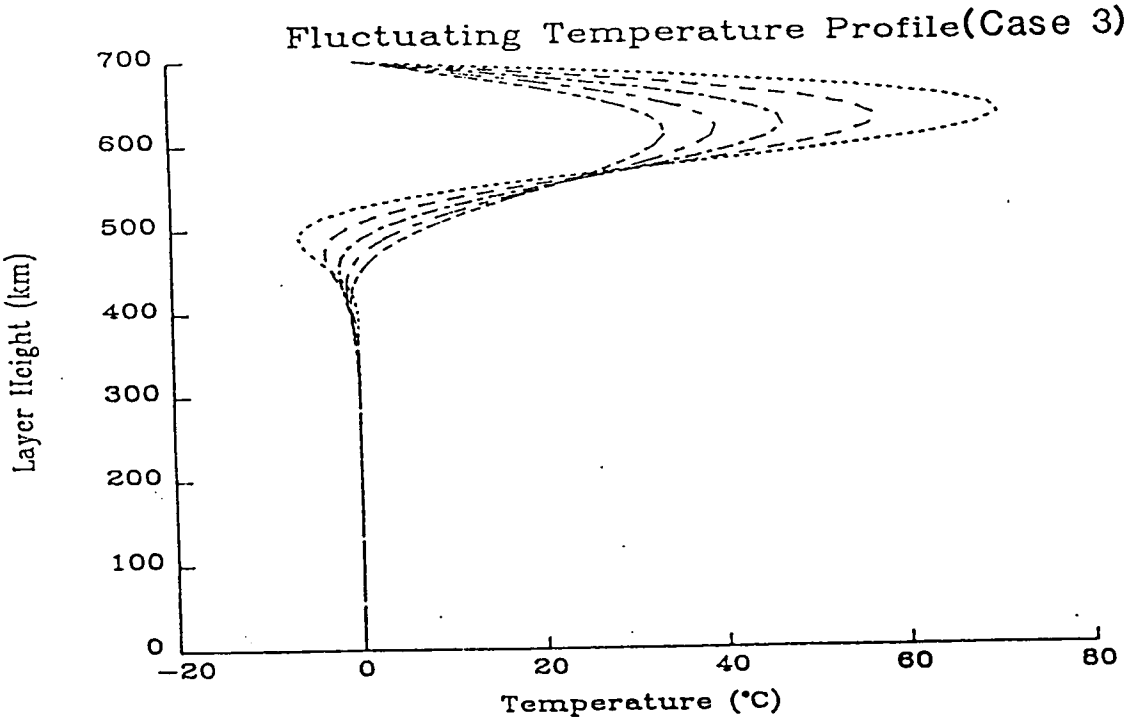
Fluctuating Temperature Profile(Case 3)
Layer Height (km)
700
600
500
400
300
200
100
0
−20
0
20
40
60
80
Temperature (°C)

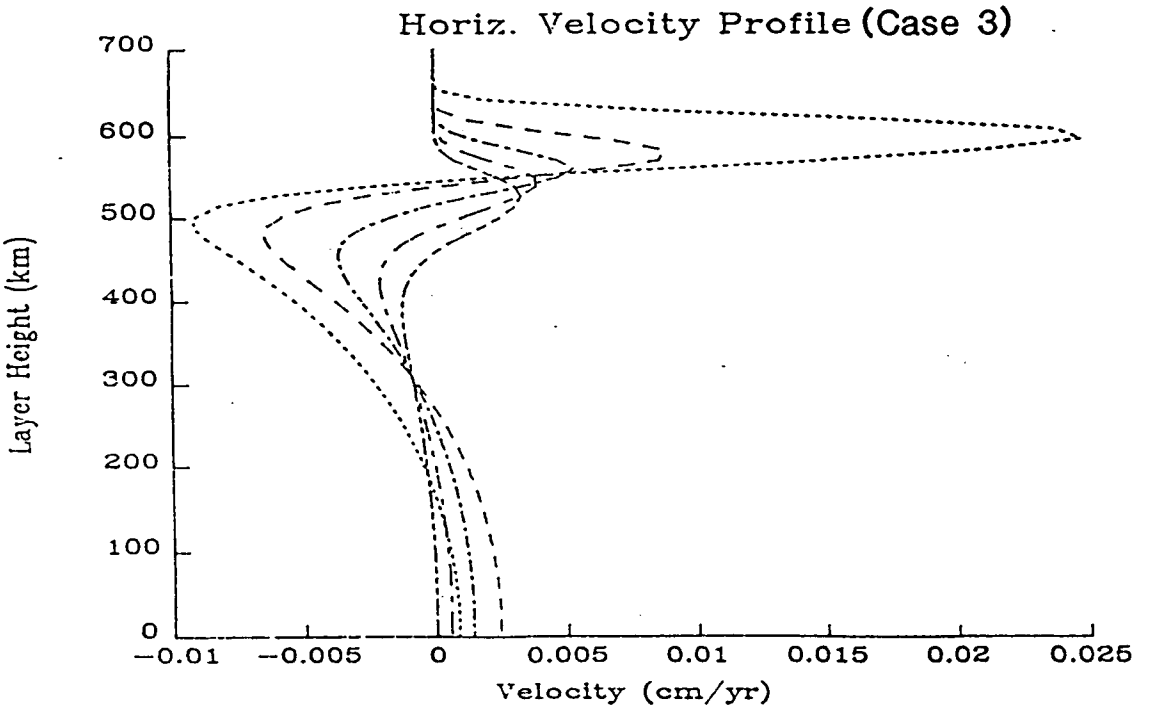
Horiz. Velocity Profile (Case 3)
Layer Height (km)
700
600
500
400
300
200
100
0
−0.01
−0.005
0
0.005
0.01
0.015
0.02
0.025
Velocity (cm/yr)

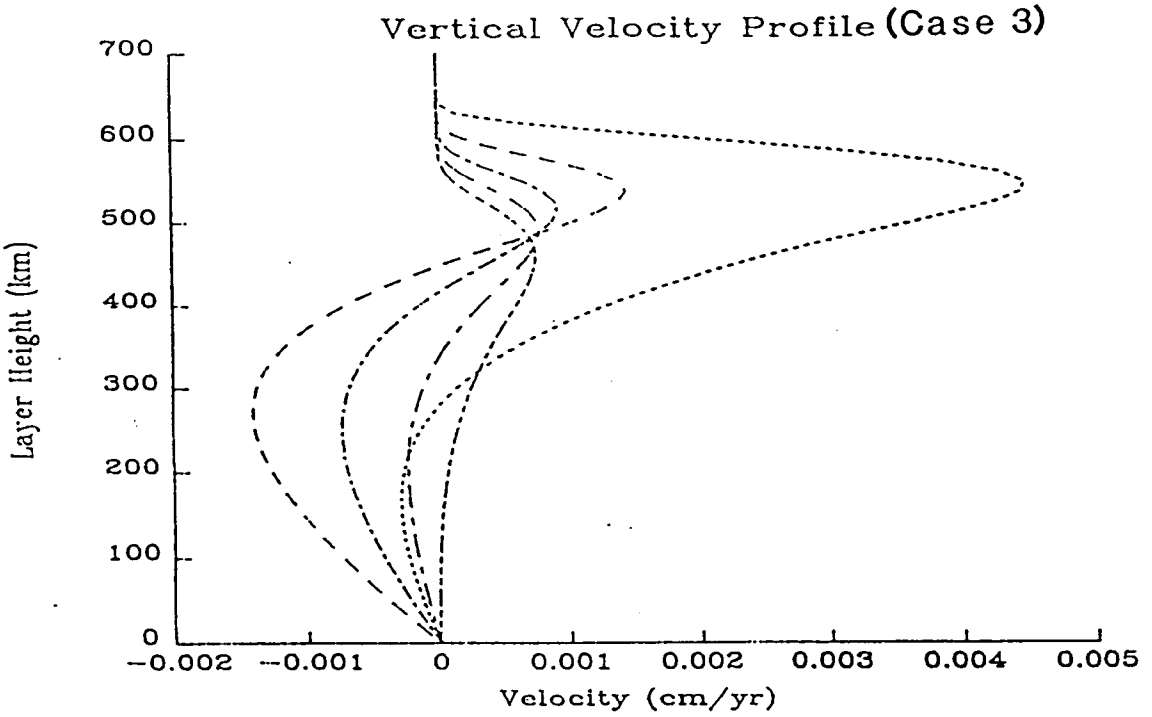
Vertical Velocity Profile (Case 3)
Layer Height (km)
700
600
500
400
300
200
100
0
−0.002
−0.001
0
0.001
0.002
0.003
0.004
0.005
Velocity (cm/yr)

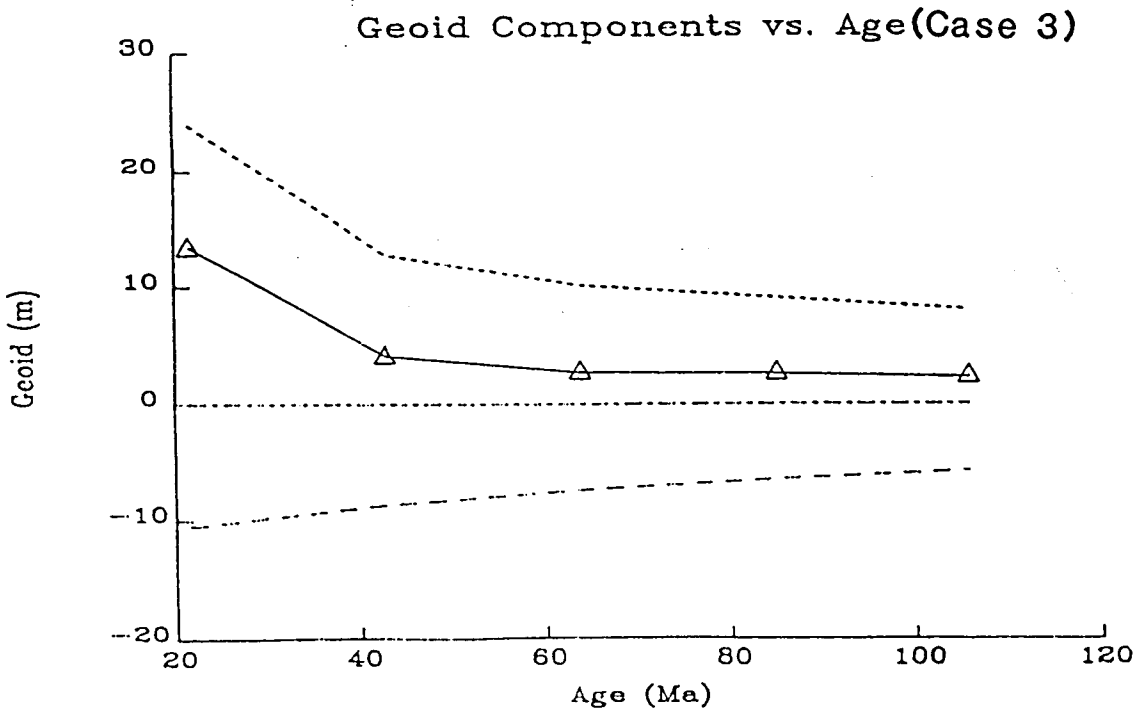
Geoid Components vs. Age (Case 3)
Geoid (m)
30
20
10
0
−10
−20
20
40
60
80
100
120
Age (Ma)

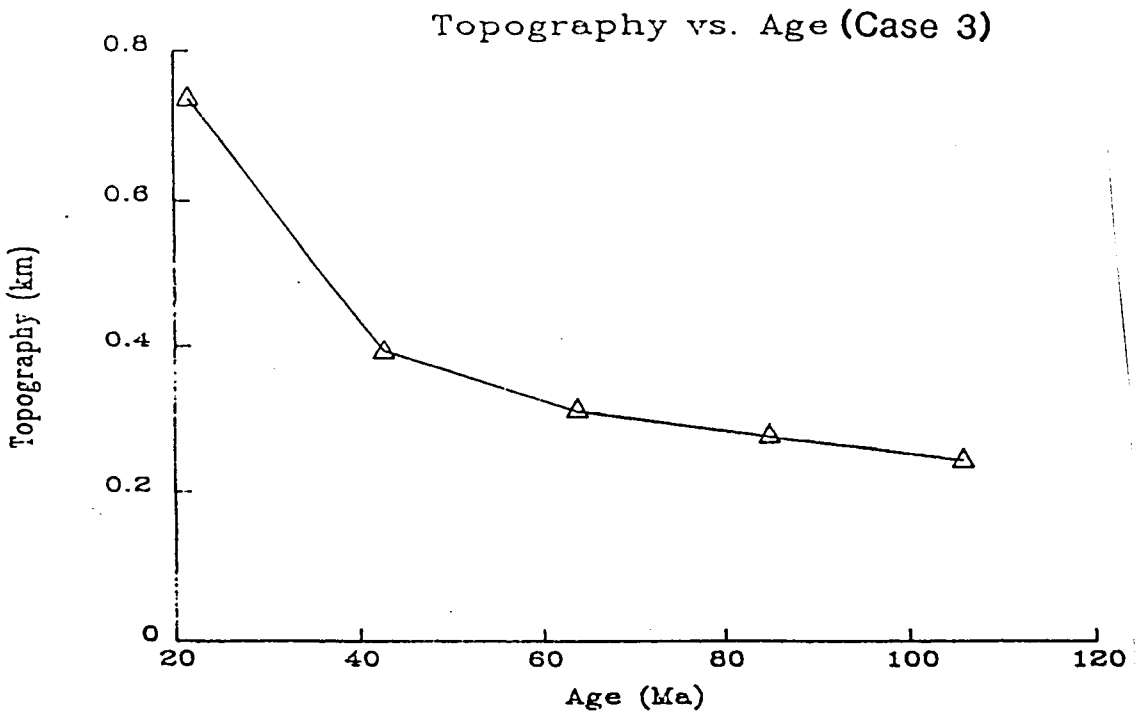
Topography vs. Age (Case 3)
Topography (km)
0.8
0.6
0.4
0.2
0
20
40
60
80
100
120
Age (Ma)

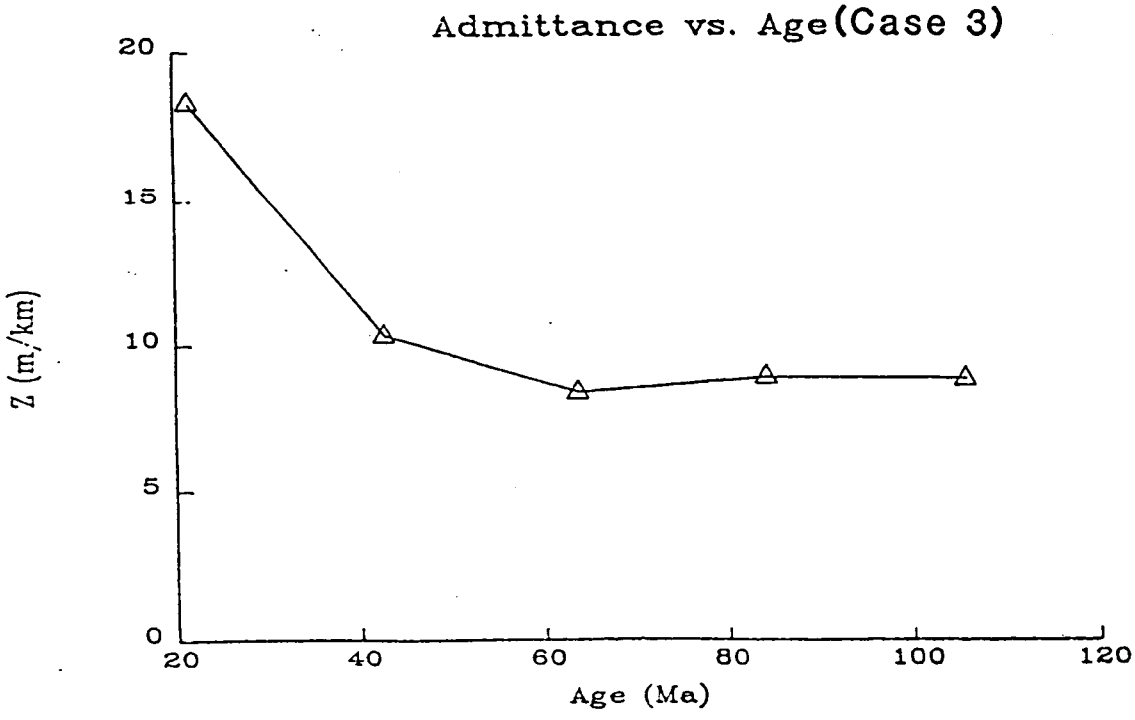
Admittance vs. Age (Case 3)
Z (m/km)
20
15
10
5
0
20
40
60
80
100
120
Age (Ma)